

Mechanical regulation of a molecular clutch defines force transmission and transduction in response to matrix rigidity

Alberto Elosegui-Artola¹, Roger Oria^{1,2}, Yunfeng Chen^{3,4}, Anita Kosmalska^{1,2}, Carlos Pérez-González^{1,2}, Natalia Castro¹, Cheng Zhu^{3,4,5}, Xavier Trepat^{1,2,6,7} and Pere Roca-Cusachs^{1,2,8}

Cell function depends on tissue rigidity, which cells probe by applying and transmitting forces to their extracellular matrix, and then transducing them into biochemical signals. Here we show that in response to matrix rigidity and density, force transmission and transduction are explained by the mechanical properties of the actin–talin–integrin–fibronectin clutch. We demonstrate that force transmission is regulated by a dynamic clutch mechanism, which unveils its fundamental biphasic force/rigidity relationship on talin depletion. Force transduction is triggered by talin unfolding above a stiffness threshold. Below this threshold, integrins unbind and release force before talin can unfold. Above the threshold, talin unfolds and binds to vinculin, leading to adhesion growth and YAP nuclear translocation. Matrix density, myosin contractility, integrin ligation and talin mechanical stability differently and nonlinearly regulate both force transmission and the transduction threshold. In all cases, coupling of talin unfolding dynamics to a theoretical clutch model quantitatively predicts cell response.

Cell function¹ and major processes in cancer² and development³ are driven by the mechanical rigidity of tissues, which cells probe through their contractile and adhesive molecular machinery. This machinery is composed of dynamic molecular bonds between the extracellular matrix (ECM), integrins, adaptor proteins and the force-generating actomyosin cytoskeleton, forming a mechanical link generally referred to as a ‘molecular clutch’^{4–6}. To sense and respond to rigidity, cells employ this molecular clutch first to transmit forces to their surrounding matrix^{5,7–9}, and then to transduce those forces into biochemical signals leading to transcriptional regulation in the nucleus¹⁰. The first step of force transmission has been modelled by introducing the dynamic properties of the clutch in computational simulations⁴, in a way that can predict the effects of adhesion mediated by different integrin types⁵. However, the fundamental prediction of such a clutch model is a biphasic force/rigidity relationship, which is in direct contradiction with the monotonically increasing curves observed in most systems^{11–15}. Further, the key molecular clutch elements driving force transmission remain to be identified. The second step of force transduction is likely to be mediated by

force-induced molecular conformational changes, which could occur at the level of ECM molecules, integrins, adaptor proteins and ion channels, among others^{16,17}. Among all potential mechanosensing molecules, the adaptor protein talin is a particularly interesting candidate because it directly links integrins to actin, is stretched as cells transmit forces to the ECM^{18,19}, and mediates cellular response to force^{20,21}. Further, talin has been observed to unfold under force *in vitro*, exposing previously cryptic binding domains to vinculin²², which then binds and is likely to be activated²³. However, if and how talin unfolding, or conformational changes in any other molecule, mediate rigidity sensing is unknown. Thus, how force transmission and transduction are coupled in response to rigidity remains unresolved.

RESULTS

Talin sets a stiffness threshold that increases force transmission and triggers force transduction

To understand how rigidity regulates both force transmission and transduction, we used talin 1^{-/-} mouse embryonic fibroblasts (with

¹Institute for Bioengineering of Catalonia, Barcelona 08028, Spain. ²University of Barcelona, Barcelona 08028, Spain. ³Woodruff School of Mechanical Engineering, Georgia Institute of Technology, Atlanta, Georgia 30332, USA. ⁴Parker H. Petit Institute for Bioengineering and Bioscience, Georgia Institute of Technology, Atlanta, Georgia 30332, USA. ⁵Coulter Department of Biomedical Engineering, Georgia Institute of Technology, Atlanta, Georgia 30332, USA. ⁶Institució Catalana de Recerca i Estudis Avançats (ICREA), Barcelona 08010, Spain. ⁷Centro de Investigación Biomédica en Red en Bioingeniería, Biomateriales y Nanomedicina, Madrid 28029, Spain.

⁸Correspondence should be addressed to P.R.-C. (e-mail: rocacusachs@ub.edu)

Received 15 October 2015; accepted 8 March 2016; published online 11 April 2016; DOI: 10.1038/ncb3336

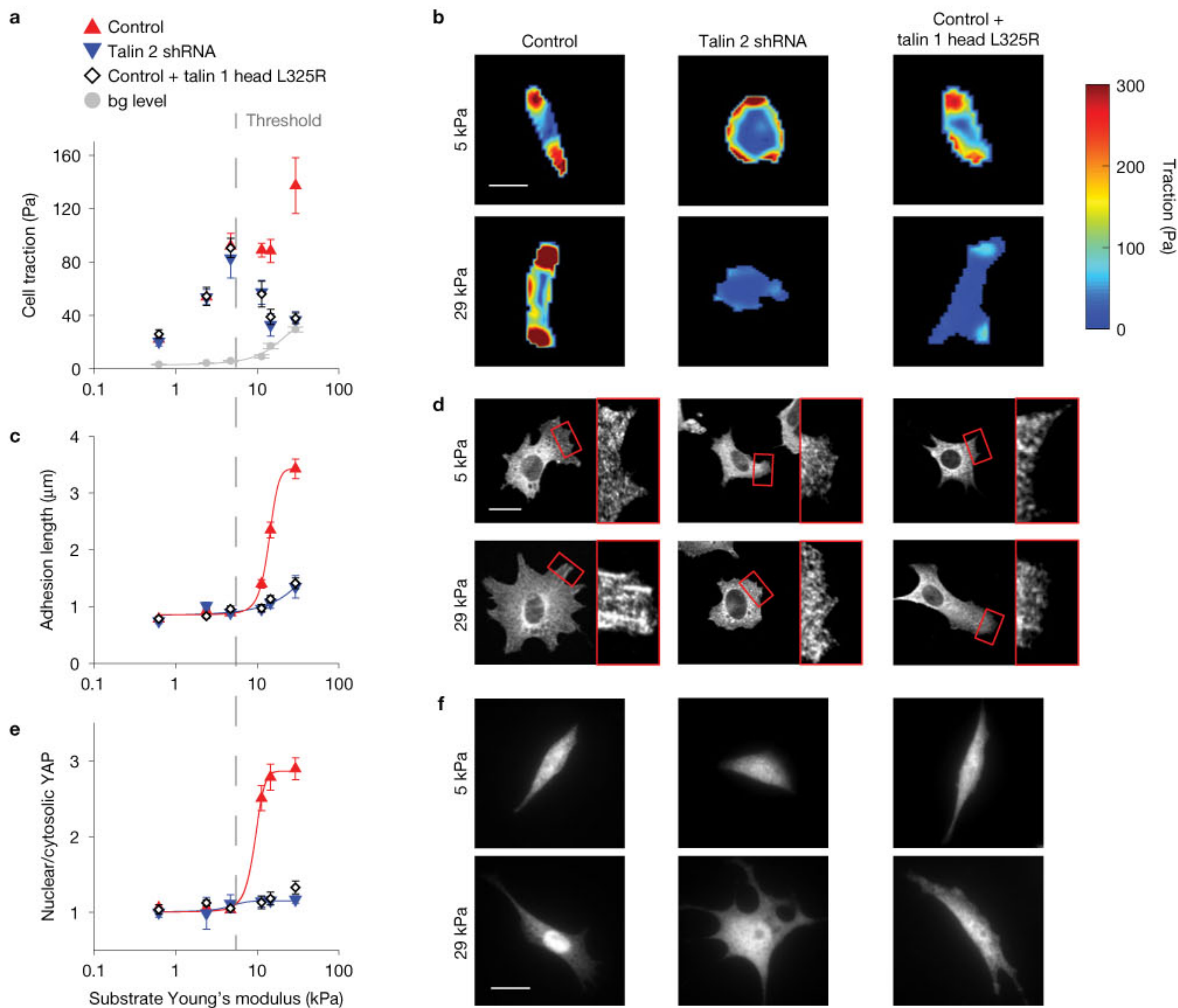


Figure 1 Talin sets a rigidity threshold that triggers increased force transmission, adhesion maturation and YAP nuclear translocation. **(a)** Average forces exerted by cells plated on fibronectin-coated polyacrylamide gels of increasing rigidity. Conditions are control (red, $n=17, 12, 35, 42, 42, 12$ cells, for increasing stiffness), talin 2 shRNA (blue, $n=10, 11, 34, 23, 25, 29$ cells) and control + talin 1 head L325R (white diamond, $n=10, 10, 24, 13, 11, 14$ cells). Data show 1 out of 14, 14 and 3 independent experiments for control, talin 2 shRNA and control + talin 1 head L325R, respectively. In grey, background (bg) noise levels show the minimum detectable force for each rigidity value (see Methods). The solid line is a fit to the experimental results. **(b)** Colour maps showing the traction forces applied by example cells in the different conditions plated on 5 and 29 kPa gels. **(c)** Quantification of vinculin adhesion length for the same conditions as in **a** (control: $n=34, 56, 76, 41, 89, 54$ adhesions for increasing stiffness measured in 9–15 cells per condition; talin 2 shRNA: $n=35, 33, 40, 36, 72, 38$ adhesions in 7–17 cells; control + talin 1 head

L325R: $n=71, 60, 43, 45, 55, 62$ adhesions in 8–14 cells). Data show one 1 of 3 independent experiments. Lines are sigmoidal fits to experimental results. **(d)** Examples of vinculin adhesions on cells plated on 5 and 29 kPa gels. Zoomed regions ($20 \times 12 \mu\text{m}$) correspond to the rectangles marked in red in the main images. **(e)** Quantification of nuclear/cytosolic YAP ratio for the same conditions as in **a** (control: $n=20, 22, 21, 29, 20, 39$ cells for increasing stiffness; talin 2 shRNA: $n=20, 20, 21, 23, 27, 23$ cells; control + talin 1 head L325R: $n=22, 27, 25, 21, 25, 34$ cells). Data show 1 out of 9, 9 and 3 independent experiments for control, talin 2 shRNA, and control + talin 1 head L325R, respectively. Lines are sigmoidal fits to experimental results. **(f)** Examples of YAP staining on cells plated on 5 and 29 kPa gels. In all quantifications **(a,c,e)**, differences between control and both talin-depleted and control + talin 1 head L325R cells were significant only above 5 kPa ($P=0.006, P<0.001, P<0.001$, two-way ANOVA). Scale bars, $20 \mu\text{m}$. Grey dashed line in **a,c,e** marks the rigidity threshold. Error bars, s.e.m.

a wild-type phenotype due to expression of talin 2 (refs 20,21) and knocked down talin 2 levels using short hairpin RNA (shRNA). We first plated control and talin 2-depleted cells on polyacrylamide gels of different rigidities. Gels were coated with the ECM protein fibronectin, to which cells adhered specifically through $\alpha_5\beta_1$ and $\alpha_v\beta_3$ integrins (Supplementary Fig. 1). Then, we measured cell-ECM force

transmission using traction force microscopy. On the softer substrates, cellular forces increased with rigidity, and talin depletion had no effect (Fig. 1a,b). However, forces sharply diverged above a threshold rigidity of 5 kPa, increasing and decreasing for control cells and depleted cells, respectively (Fig. 1a,b). In control cells, this threshold coincided with the growth of focal adhesions rich in vinculin (Fig. 1c,d) and

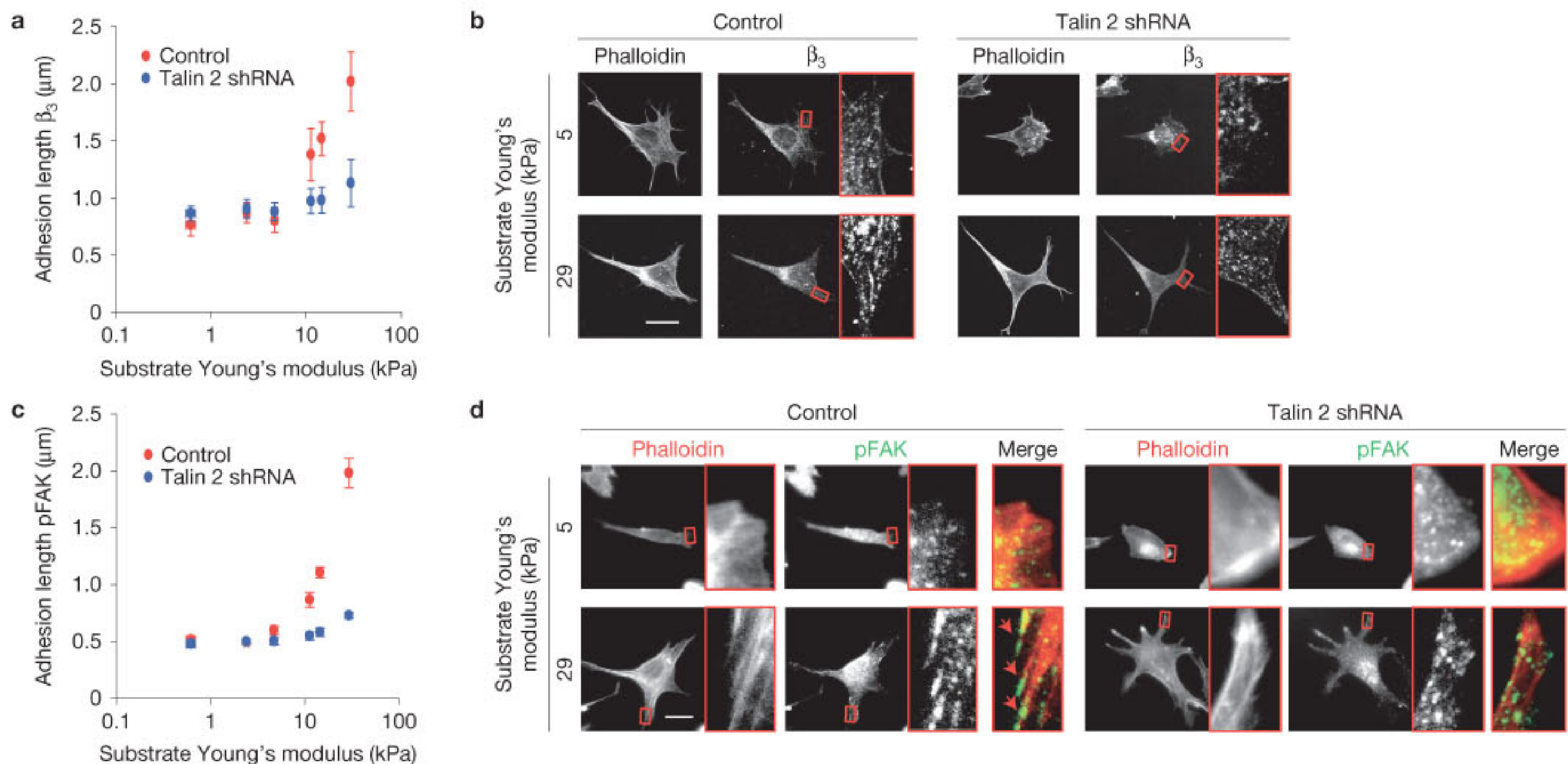


Figure 2 Talin depletion affects β_3 ligation, FAK phosphorylation and stress fibre formation only above the stiffness threshold. **(a)** Quantification of adhesion length from staining images of ligand-bound β_3 for control (red) and talin 2 shRNA cells (blue) as a function of substrate stiffness. Control: $n=27, 63, 47, 43, 63, 61$ adhesions for increasing stiffness, measured in 8–10 cells. Talin 2 shRNA: $n=28, 31, 40, 31, 27, 31$ adhesions in 8–9 cells. Data show 1 out of 3 independent experiments. Significant differences were found between control and depleted cells only above 5 kPa ($P<0.001$, two-way ANOVA). **(b)** Examples of phalloidin and ligand-bound β_3 integrin stainings in control and talin 2 shRNA cells plated on 5 and 29 kPa gels. Insets ($6 \times 10 \mu\text{m}$) show magnifications of the zones marked in red. **(c)** Quantification of adhesion length

from staining images of phosphorylated FAK (pFAK) for control (red) and talin 2 shRNA cells (blue) as a function of substrate stiffness. Control: $n=24, 27, 28, 25, 30, 26$ adhesions for increasing stiffness, measured in 8–9 cells. Talin 2 shRNA: $n=24, 31, 33, 24, 24$ adhesions in 8–19 cells. Data show 1 out of 3 independent experiments. Significant differences were observed only above 5 kPa ($P<0.001$, two-way ANOVA). **(d)** Examples of phalloidin and pFAK stainings in control and talin 2 shRNA cells plated on 5 and 29 kPa gels. Insets ($6 \times 10 \mu\text{m}$) show magnifications of the zones marked in red. In the merged images, phalloidin is red and pFAK is green. Red arrows show pFAK-positive focal adhesions where stress fibres terminate. Scale bars, 20 μm . Error bars, s.e.m.

with the activation (nuclear translocation) of the mechanosensitive transcriptional regulator YAP¹⁰ (Fig. 1e,f). In contrast, talin-depleted cells spread on gels, but did not develop focal adhesions or localize YAP to the nucleus at any rigidity (Fig. 1c–f). To confirm those results, we blocked talin function in control cells by a mechanism alternative to shRNA. We transfected cells with a dominant negative talin head mutant (L325R) that displaces endogenous talin for integrin binding, but does not activate integrins or link them to the cytoskeleton²⁴. On stiff substrates, increasing levels of talin head L325R expression progressively reduced force transmission to the levels of talin-depleted cells (Fig. 1a,b and Supplementary Fig. 2), and abrogated adhesion growth and YAP nuclear translocation as expected (Fig. 1c–f). In contrast and consistently with shRNA results, talin head L325R expression had no effect on soft substrates (Fig. 1a–f and Supplementary Fig. 2). Further reinforcing the importance of the talin-dependent threshold, it also marked the recruitment of integrins and phosphorylated FAK to adhesions (Fig. 2a–d and Supplementary Fig. 3), and the association of adhesions to stress fibres (Fig. 2c,d). Those results provide important insights into the two steps required for rigidity sensing, force transmission and force transduction. Regarding force transmission, we show that the core long-standing prediction of the clutch adhesion model (a biphasic force/rigidity curve, so far only partially observed in neuronal

filopodia⁴) is correct, but fully unveiled only in the absence of talin-mediated reinforcement. Regarding force transduction, we show that it is triggered above a rigidity threshold in a talin-dependent manner, leading to adhesion growth, downstream biochemical signalling and YAP activation.

Regulation of talin unfolding by a molecular clutch can explain force transmission and transduction in response to rigidity

We then assessed whether the effects of rigidity and talin could be mediated by known force regulators such as myosin phosphorylation and cell spreading. Whereas myosin phosphorylation levels slightly fluctuated as a function of substrate stiffness and talin depletion (Supplementary Fig. 4), those fluctuations did not correlate with transmitted forces. As reported previously⁵, cell areas increased with rigidity, reaching a plateau at about 5 kPa (Supplementary Fig. 4). However, no significant differences were measured between control and talin-depleted cells. Further, the threshold rigidity leading to adhesion growth, YAP activation and force decrease in talin-depleted cells was not associated with cell spreading changes. Thus, neither myosin phosphorylation nor cell spreading could account for the effects of talin, or the rigidity threshold.

Alternatively, the rigidity threshold may result from the regulation of talin unfolding by the ECM–integrin–talin–actin clutch. To

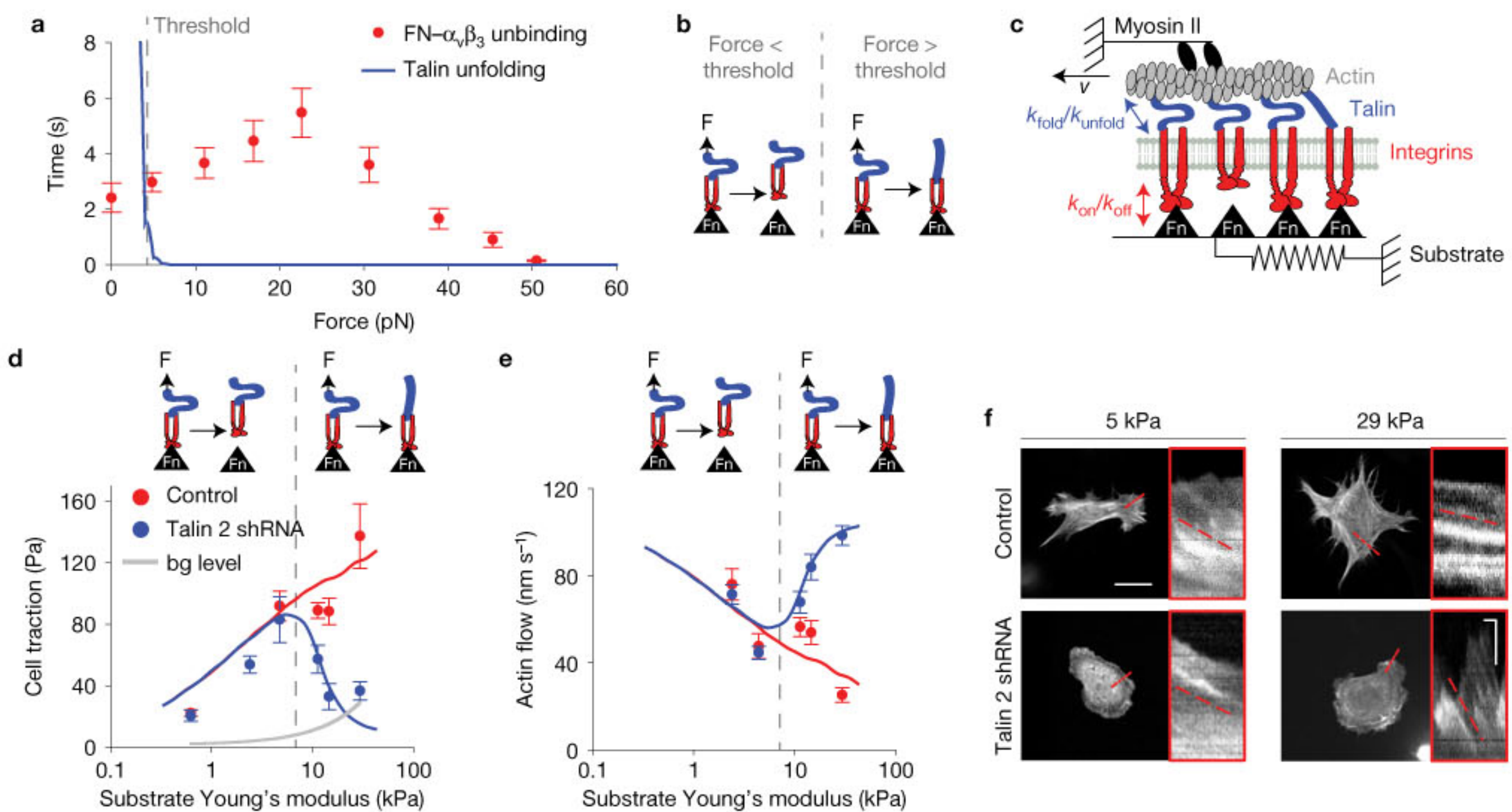


Figure 3 The balance between clutch unbinding and talin unfolding predicts the force/rigidity curves and the rigidity threshold for mechanotransduction. **(a)** Measured average lifetime of fibronectin (FN)- $\alpha_v\beta_3$ bonds as a function of force (red points). $n = 20, 29, 120, 162, 176, 146, 162, 61, 27$ traces for increasing force pooled from 6 independent experiments. The threshold force enabling talin unfolding is shown in grey. **(b)** Schematic diagram depicting how force leads to integrin (red) unbinding below the threshold, but talin (blue) unfolding above. **(c)** Molecular clutch model of force transmission. Myosin motors pull with a speed v on actin filaments, which are connected to a compliant substrate (represented as a linear elastic spring of varying rigidity) through several parallel molecular clutches. Once clutches bind to the substrate (with a binding rate k_{on}), force is loaded progressively as the fibre retracts, determining the unbinding rate k_{off} and the unfolding/refolding rates k_{unfold}/k_{fold} according to the profiles

in **a** (see Supplementary Note). **(d)** Experimental force data from Fig. 1a superimposed to model predictions with/without talin unfolding (solid red and blue lines, respectively). The grey line shows the minimum detection level. **(e)** Quantification of actin flow speeds and model predictions (solid lines) for cells plated on fibronectin-coated polyacrylamide gels of increasing rigidity. Conditions are control (red, $n = 23, 19, 21, 19, 20$ traces for increasing stiffness, measured in 10–11 cells) and talin 2 shRNA (blue, $n = 24, 24, 22, 22, 39$ traces in 10–17 cells). Data show 1 out of 3 independent experiments. **(f)** Examples of control and talin 2 shRNA cells transfected with LifeAct-GFP and plated on 5 and 29 kPa gels. Insets are kymographs showing the movement of actin features along the lines marked in red. The slope of the traces created by the features (marked with dashed lines) was used to calculate actin speed. Scale bars, 20 μ m in the main images and 20 s/2 μ m (x/y axes) in the kymographs. Error bars, s.e.m.

investigate this, we compared how force affects the unfolding time of single talin molecules (previously measured²⁵) versus the unbinding time of single fibronectin-integrin bonds (both for $\alpha_5\beta_1$ integrins, previously measured²⁶, and $\alpha_v\beta_3$ integrins, measured here in Fig. 3a). For clutches mediated by either integrin type, at low forces integrins unbind faster, releasing force transmission and preventing talin unfolding. However, unfolding becomes faster than unbinding above a threshold force (Fig. 3b). This threshold force for unfolding could be further modulated by unbinding events in integrin-talin-actin bonds, which would decrease overall clutch unbinding times, or by load sharing between talin and other adaptor molecules, which would decrease the load on talin and slow unfolding. Independently of its specific value, a force threshold for talin unfolding thus emerges, which may mediate the rigidity threshold observed in Fig. 1.

To evaluate this possibility, we developed a computational approach to couple talin unfolding to a clutch model⁵ (see Supplementary Note for details). This model considers a given number of myosin motors progressively pulling on an actin fibre, which is bound to a deformable substrate through molecular clutches formed by adaptor proteins (such as talin), integrins and fibronectin (Fig. 3c). Once the

clutches bind according to a given binding rate, fibre contraction deforms the substrate and results in progressive force loading, which is slow or fast on soft or stiff substrates, respectively. This force loading leads to either clutch unbinding or talin unfolding. If talin unfolds, vinculin binds, leading to adhesion reinforcement and growth²⁰ and integrin recruitment. In the absence of talin unfolding, integrins are not recruited, but force is still assumed to be transmitted between integrins and actin through other adaptor proteins²⁷.

If talin unfolding is not considered, we recapitulate the fundamental prediction of the clutch model⁴, that is, a biphasic force/rigidity curve with an optimal rigidity of maximum force transmission (Fig. 3d, blue line). Below the optimal rigidity, force loads so slowly that clutches unbind from the ECM before exerting significant forces. Above the optimal rigidity, force loading is so fast that clutches unbind from the ECM before other clutches have time to bind, reducing cooperativity and decreasing total force transmission. The presence of talin does not affect the curve at low rigidities, where forces are too low to allow unfolding. However, above a rigidity threshold, force loading becomes fast enough to allow talin unfolding before integrin unbinding. This leads to vinculin binding and integrin

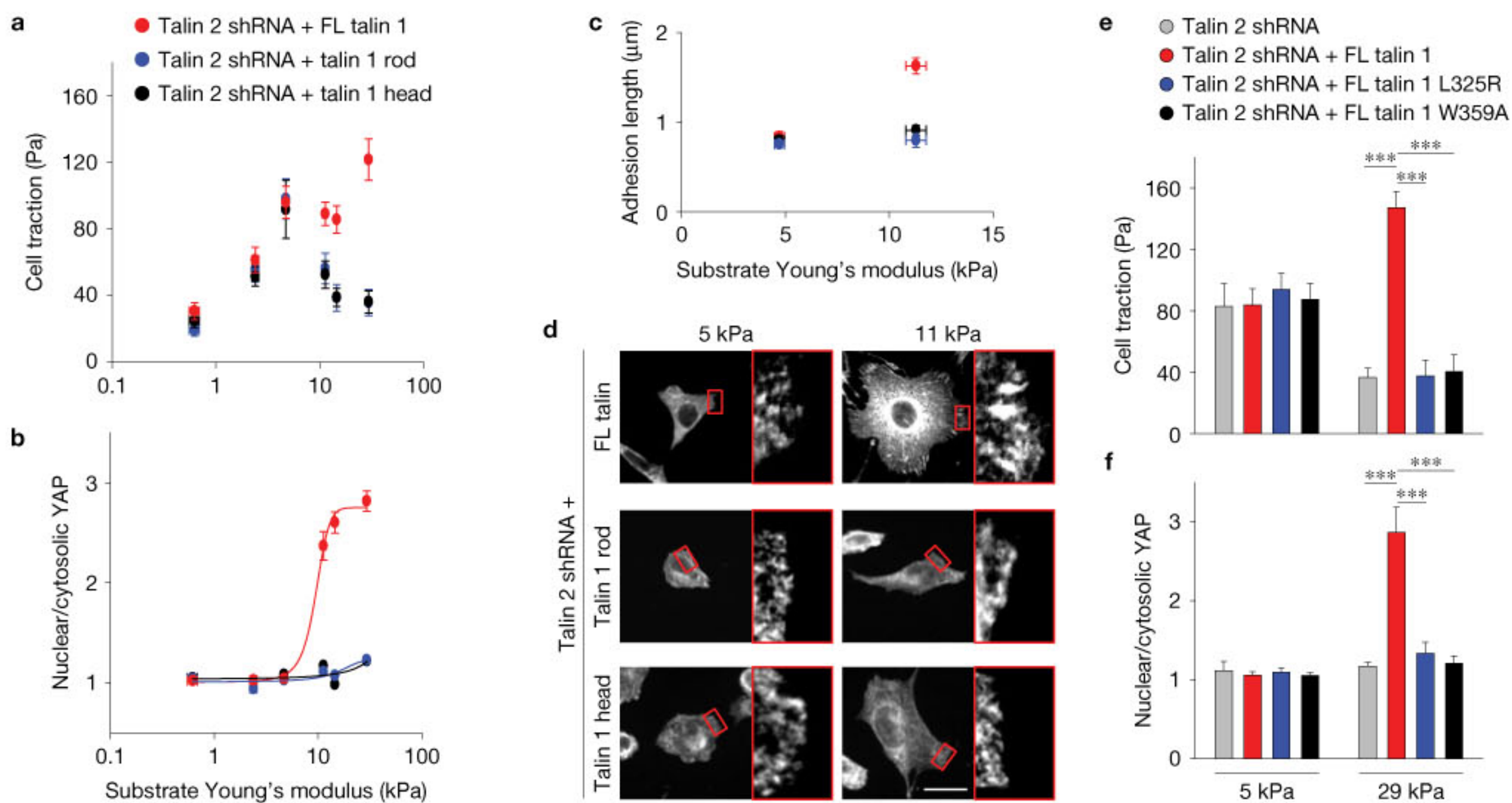


Figure 4 The rigidity threshold requires an intact integrin–cytoskeletal link mediated by full-length talin. **(a–c)** Average forces, nuclear/cytosolic YAP ratios and vinculin adhesion lengths for talin 2 shRNA cells plated on fibronectin-coated gels of increasing rigidity and co-transfected with different talin constructs. Constructs are: full-length (FL) talin 1 (for increasing stiffness, $n=10, 11, 14, 16, 20, 16$ cells for forces, $n=20, 22, 21, 23, 53, 49$ cells for YAP ratios, and $n=59, 63$ adhesions measured in 9–10 cells for adhesion lengths); talin 1 rod (for increasing stiffness, $n=10, 13, 14, 10, 12, 10$ cells for forces, $n=21, 21, 20, 22, 23, 24$ cells for YAP ratios, and $n=49, 43$ adhesions measured in 8–10 cells for adhesion lengths); talin 1 head (for increasing stiffness, $n=10, 12, 11, 13, 11, 13$ cells for forces, $n=20, 21, 20, 32, 23, 26$ cells for YAP ratios, and $n=49, 41$ adhesions measured in 8–10 cells for adhesion lengths). Significant differences between FL talin and the other two plasmids were found for forces,

YAP ratios and adhesion lengths only above 5 kPa ($P=0.012$, $P<0.001$, two-way ANOVA). Data show 1 out of 4 independent experiments for forces, 3 for YAP and adhesion length. **(d)** Examples of vinculin stainings for cells plated on gels with different rigidities for the conditions indicated. Scale bar, 20 μm . Insets are 10 \times 6 μm . **(e)** Quantification of traction forces exerted on substrates of 5 kPa and 29 kPa by talin 2 shRNA cells (grey) and talin 2 shRNA cells co-transfected with FL talin 1 (red), FL talin 1 L325R (blue) and FL talin 1 W359A (black). From left to right, $n=34, 17, 11, 12, 29, 12, 13, 11$ cells. **(f)** Quantification of nuclear/cytosolic YAP ratio for the same conditions. From left to right, $n=21, 24, 23, 26, 23, 20, 28, 22$ cells. Significant differences were observed between talin 2 shRNA+FL talin 1 and all other conditions at 29 kPa but not 5 kPa (** $P<0.001$, two-way ANOVA). Data show 1 out of 3 independent experiments in **e** and **f**. Error bars, s.e.m.

recruitment, increasing integrin binding and force transmission, and eliminating the biphasic relationship (Fig. 3d, red line). In all cases, force transmission resists actin contraction, leading to a negative correlation between force and actin flow (Fig. 3e). The model closely reproduced our force measurements (see Supplementary Table 1 and Supplementary Note for model parameters and assumptions). Confirming the validity of the clutch hypothesis, actin flows correlated negatively with forces, and could also be reproduced by the model using the same parameters (Fig. 3e,f, and Supplementary Videos 1 and 2). Thus, control of talin unfolding by force transmitted through the ECM–actin clutch can explain how rigidity regulates both force transmission, and the threshold for mechanotransduction.

The rigidity threshold is mediated by talin unfolding under force and subsequent vinculin binding

We then carried out several experiments to validate this mechanism molecularly. First, we rescued talin 2-depleted cells with either full-length (FL) talin 1 or two separate fragments, the talin 1 rod and the talin 1 head. FL talin 1 rescued rescue force generation, adhesion growth and YAP localization to control levels, confirming that talin

1 and 2 had the same effect^{20,21}. However, neither the talin rod nor the head rescued the phenotype of depleted cells (Fig. 4a–d). As the talin head is sufficient to activate integrins^{21,28}, this shows that integrin activation without force transmission through talin was not sufficient to trigger a rigidity response. Confirming this, FL talin mutants that do not bind integrins (W359A) or bind but do not activate integrins (L325R)²⁴ did not rescue force generation or YAP localization above the rigidity threshold (Fig. 4e,f). Second, we generated a talin mutant (FL talin 1 IVVI) containing four point mutations shown to increase the force required for talin unfolding (that is, the force where unfolding rates become faster than refolding rates) from 5 to 8 pN (ref. 25). This should increase the threshold rigidity for unfolding, displacing the effect of talin to higher rigidities. Accordingly, cells rescued with IVVI instead of wild-type talin diverged from talin-depleted cells (in terms of force generation, adhesion growth and YAP translocation) at a higher rigidity (15 instead of 11 kPa; Fig. 5a–d). This result demonstrates that adhesion growth and YAP activation in response to rigidity are triggered by talin unfolding, and that this response can be regulated by modulating talin mechanical stability.

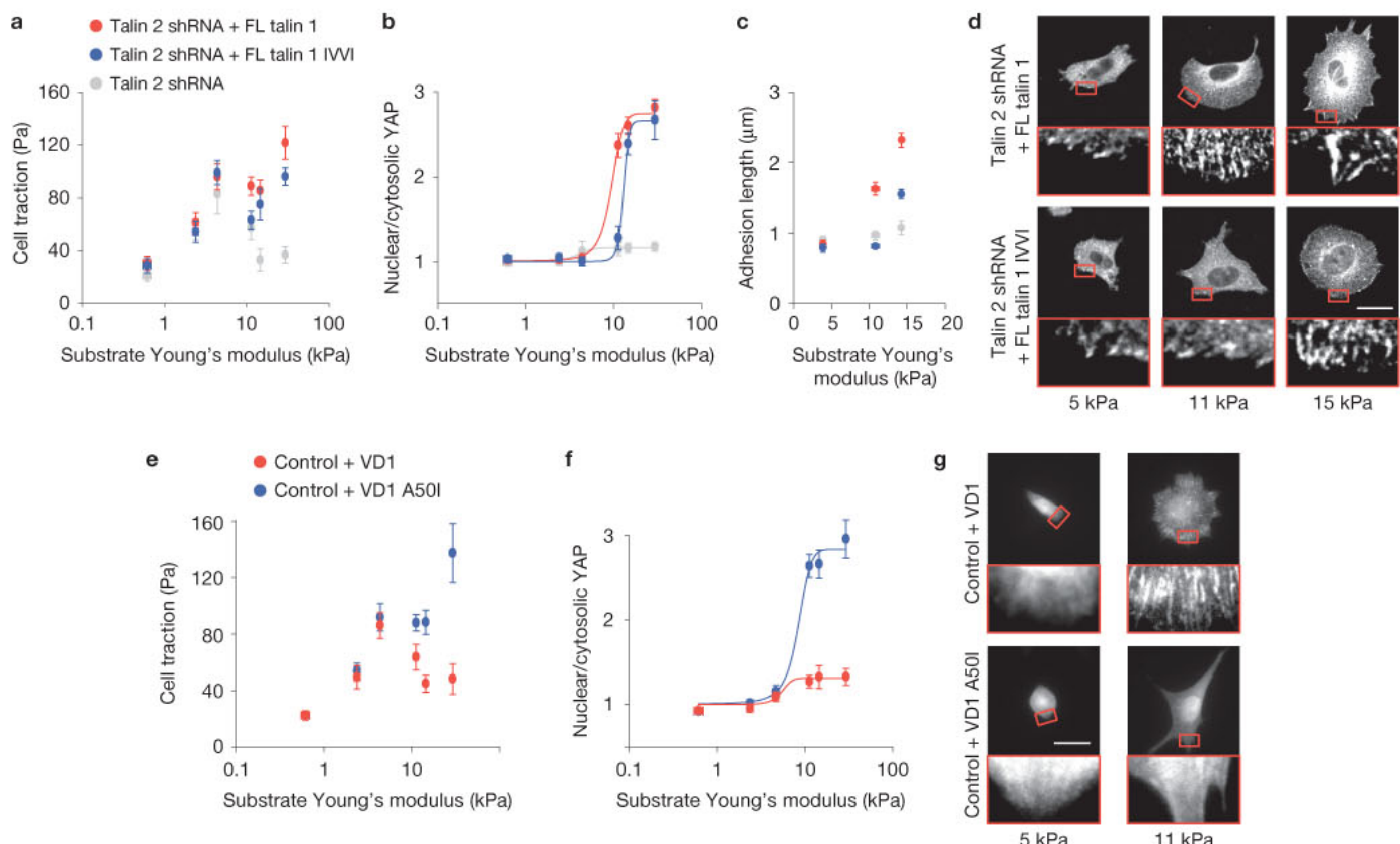


Figure 5 The rigidity threshold is mediated by talin unfolding under force and subsequent vinculin binding. **(a–c)** Average forces, nuclear/cytosolic YAP ratios and vinculin adhesion lengths exerted on fibronectin-coated gels of increasing rigidity by talin 2 shRNA cells co-transfected with different constructs. Conditions are: no co-transfection (grey, for increasing stiffness, $n=10, 11, 34, 23, 29$ cells for forces, $n=20, 20, 21, 23, 27$ cells for YAP ratios, and $n=40, 36, 72$ adhesions measured in 10–17 cells for adhesion lengths); FL talin 1 (red, for increasing stiffness, $n=10, 11, 14, 16, 20, 16$ cells for forces, $n=20, 22, 21, 23, 53, 49$ cells for YAP ratios, and $n=59, 63, 59$ adhesions measured in 9–10 cells for adhesion lengths); FL talin 1 IVVI (blue, for increasing stiffness, $n=10, 13, 14, 19, 15, 15$ cells for forces, $n=22, 23, 21, 21, 22, 22$ cells for YAP ratios, and $n=43, 30, 85$ adhesions measured in 7–14 cells for adhesion lengths). Significant differences between FL talin and FL talin IVVI were found at 11 kPa for all measurements ($P=0.034$, $P<0.001$, $P<0.001$, two-way ANOVA).

ANOVA). Data show 1 out of 3 independent experiments. **(d)** Examples of vinculin stainings for cells plated on gels with different rigidities for the conditions indicated. **(e,f)** Average forces and nuclear/cytosolic YAP ratios exerted on fibronectin-coated gels of increasing rigidity by control cells transfected with different constructs. Constructs are VD1 (red, for increasing stiffness, $n=10, 13, 13, 13, 16, 15$ cells for forces, and $n=26, 20, 30, 29, 21, 32$ cells for YAP ratios); VD1 A50I (blue, for increasing stiffness, $n=11, 14, 10, 13, 16, 18$ cells for forces, and $n=22, 21, 21, 23, 22, 24$ cells for YAP ratios). Significant differences between VD1 and VD1 A50I transfection were found for all measurements above 11 kPa but not below ($P=0.006$, $P<0.001$, two-way ANOVA). Data show 1 out of 3 independent experiments. **(g)** Examples of VD1 and VD1 A50I fluorescence distribution for cells plated on gels with different rigidity for the conditions indicated. Scale bars, 20 μm. Insets are 10 × 6 μm. Error bars, s.e.m.

We then evaluated whether the effect of talin unfolding was mediated by vinculin binding. We transfected control cells with VD1, a vinculin fragment that is dominant over endogenous vinculin for talin binding²⁹ but prevents normal vinculin function^{30,31} owing to the lack of remaining functional domains. Blocking vinculin function through VD1 transfection had the same effect as talin depletion, that is, forces decreased at high rigidities, and YAP remained cytosolic (Fig. 5e,f and Supplementary Fig. 5). VD1 formed large focal adhesions above but not below the rigidity threshold (Fig. 5g), confirming that vinculin binding was specifically triggered above the threshold. As a negative control, transfection of a VD1 mutant (A50I) with reduced affinity for talin had no effect (Fig. 4e–g). Neither VD1 nor VD1 A50I had any effect on talin-depleted cells (Supplementary Fig. 5). Collectively, those data show that force unfolds talin above a rigidity threshold, leading to vinculin binding, adhesion growth and YAP translocation to the nucleus.

The molecular determinants of the clutch regulate force transmission and transduction

Finally, we analysed the role of different clutch molecular determinants predicted to regulate force transmission^{32,33}. First, if available clutches are decreased (by reducing substrate fibronectin coating density, see Supplementary Fig. 6), overall force transmission should be reduced. However, force loading per clutch increases because actomyosin contractility is distributed among fewer clutches, triggering talin unfolding, reinforcement and YAP translocation at a lower rigidity threshold. As the rigidity corresponding to peak force transmission in depleted cells is also determined by force loading^{32,33}, it also shifts to a lower value. If fibronectin coating is increased, the inverse effect is expected. Second, reducing the binding rate of integrins (by partially blocking integrins with the GPen peptide) should reduce the number of bound clutches, leading to effects similar to those of reducing fibronectin coating. However, in this case

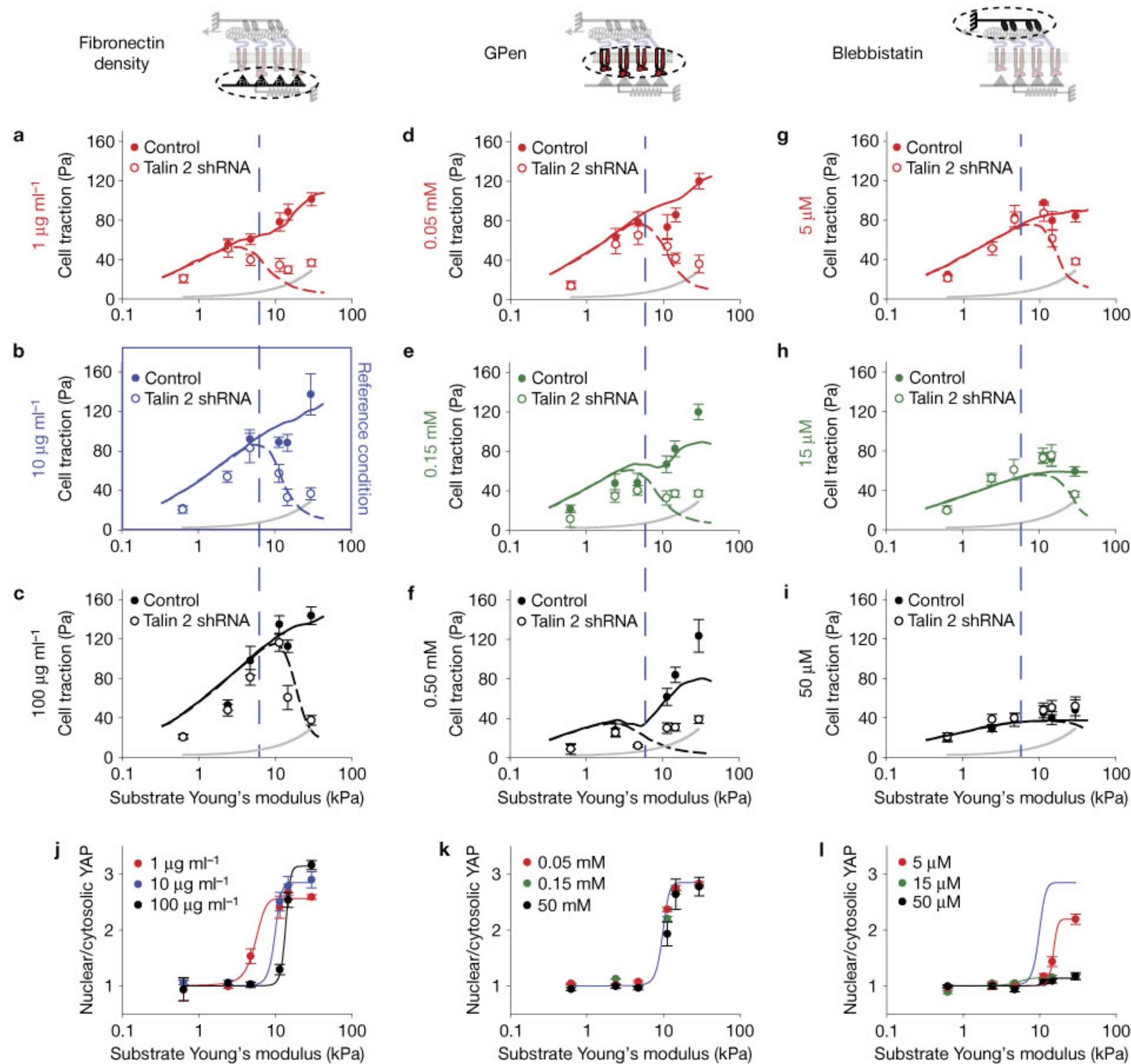


Figure 6 The elements of the molecular clutch tune force transmission and the rigidity threshold required for talin unfolding and YAP nuclear translocation. (a–c) Average cell traction forces on gels of varying concentration of fibronectin coating. Solid and dashed lines show model predictions with and without talin unfolding, respectively, after adjusting the parameter n_t (number of fibronectin molecules). (a) 1 $\mu\text{g ml}^{-1}$, $n_t = 750$, (b) 10 $\mu\text{g ml}^{-1}$, $n_t = 1200$ (blue, reference condition from Fig. 1), and (c) 100 $\mu\text{g ml}^{-1}$, $n_t = 1650$ ($n \geq 10$ cells per condition). (d–f) The same quantification for cells with different concentrations of the integrin blocking peptide GPen. The parameters adjusted were k_{ont} (true integrin binding rate) and d_{add} (number of integrins added after each reinforcement step). (d) 0.05 mM, $k_{\text{ont}} = 1.9 \times 10^{-4} \mu\text{m}^2 \text{s}^{-1}$, $d_{\text{add}} = 24$, (e) 0.15 mM, $k_{\text{ont}} = 1.5 \times 10^{-4} \mu\text{m}^2 \text{s}^{-1}$, $d_{\text{add}} = 10$, and (f) 0.50 mM, $k_{\text{ont}} = 0.9 \times 10^{-4} \mu\text{m}^2 \text{s}^{-1}$, $d_{\text{add}} = 6$ ($n \geq 10$ cells per condition). (g–i) The same quantification for cells with different concentrations of the myosin

inhibitor blebbistatin. The parameter adjusted was n_m (number of myosin motors). (g) 5 μM , $n_m = 500$, (h) 15 μM , $n_m = 300$, and (i) 50 μM , $n_m = 180$ ($n \geq 10$ cells per condition). The dashed vertical blue lines show the position of the rigidity threshold in reference conditions (no treatment, 10 $\mu\text{g ml}^{-1}$ fibronectin coating). In all force quantifications, the grey lines show the minimum detectable force level, which increased with rigidity and reached the values measured for talin-depleted cells at high rigidities. Thus, those values reflect the detection level rather than actual generated forces, which were likely to be below the detection threshold. (j–l) Quantification of the nuclear/cytosolic YAP ratio for control cells in the three different concentrations of fibronectin (j), GPen (k) and blebbistatin (l) ($n \geq 20$ cells per condition). The blue lines show YAP activation levels in reference conditions; the other lines are sigmoidal fits to the experimental results. See Supplementary Table 3 for sample numbers and statistical analysis. Error bars, s.e.m.

integrins are partially blocked, impairing reinforcement and adhesion growth on talin unfolding. This counters the effect of the increased loading per integrin, leading to reduced overall force transmission and a shift to lower rigidities of the peak force in depleted cells, but no major change in the threshold rigidity for reinforcement

and YAP translocation. Third, decreasing myosin contractility (by using different concentrations of blebbistatin) should reduce force loading, increasing the rigidity threshold for talin unfolding and YAP activation. Similarly, the force peak in depleted cells should shift to higher rigidities, and reduce its height. All of those predictions

were verified experimentally (Fig. 6). Although model predictions did not always provide an exact quantitative match, they consistently predicted the shifts in overall forces, the rigidity threshold at which forces diverge between control and depleted cells, and the position of the force peak in depleted cells. Those predictions were obtained by adjusting only the relevant parameters in each case: number of fibronectin molecules (n_f) for fibronectin coating (Fig. 6a–c), integrin binding and recruitment rates (k_{on} and d_{add}) for GPen (Fig. 6d–f), and number of myosin motors (n_m) for blebbistatin (Fig. 6g–i). In all cases, YAP localized to the nucleus at the same rigidity threshold where measured forces diverged between control and depleted cells (Fig. 6j,k,l). Thus, force transmission was systematically modulated by the molecular determinants of the clutch, leading to mirror shifts in the thresholds for talin unfolding and YAP activation.

DISCUSSION

Our results unveil the mechanisms by which microenvironment rigidity regulates both force transmission and transduction, and reconcile previous findings. Indeed, even though cell–ECM adhesion is widely accepted to be mediated by a molecular clutch mechanism, its predicted biphasic force/rigidity relationship is inconsistent with monotonically increasing trends observed in most systems^{11–14}. Here we show that the biphasic force/rigidity relationship is normally masked by talin-mediated reinforcement and adhesion growth, and is fully unveiled only on talin depletion. This depletion allowed us to test the molecular determinants of force transmission, revealing that its regulation by rigidity, ECM coating density, cell contractility or integrin activity fully abides by the clutch model first proposed eight years ago^{4,32,33}. This leads to interesting and counter-intuitive results, such as that decreasing ECM coating enhances the mechanical response (Fig. 6j), or that mild myosin inhibition (5–15 μM) increases cell–ECM force transmission in talin-depleted cells for a specific rigidity range (10–15 kPa, Fig. 6g,h). This is because although overall contractility is reduced, the force peak is shifted to higher rigidities.

Whereas in this work we focused on fibronectin substrates bound to cells through $\alpha_5\beta_1$ - and $\alpha_v\beta_3$ -mediated catch bonds, we note that the emergence of a threshold for talin unfolding does not require catch bonds. Even if integrins behaved as slip bonds, a rigidity threshold would occur if the force/unbinding and force/unfolding curves crossed at a given force. Given the extremely steep decay in talin unfolding times as a function of force (Fig. 3a), this is likely to happen in most scenarios. Further, talin unfolding at low forces would also be prevented by very fast refolding rates, a factor that was also included in our modelling. Thus, the force and rigidity threshold for talin unfolding is likely to apply in many physiological scenarios, and could be regulated by several factors. First, clutch unbinding events at the level of integrin–talin–actin bonds could increase overall clutch unbinding rates, displacing the threshold to higher forces/rigidities. This effect would alter the specific values of model output, but would not modify the overall trends of the force/rigidity curves with and without talin, the presence of a rigidity threshold for unfolding, or the regulation of this threshold by the different factors. Second, load sharing between talin and other adaptor proteins could reduce the force experienced by individual talin molecules, also increasing the threshold. Indeed, the best fit of our model was obtained by setting the fraction of force on talin to 7.3% (see Supplementary Table 1),

suggesting that talin experiences only a small fraction of the load transmitted by integrins (of the order of a few piconewtons). This is consistent with recently measured tension levels across single talin molecules within cells¹⁸, and with the observation that talin depletion did not affect force transmission at low rigidities (Fig. 1). Collectively, those data support the notion that the soft properties of talin¹⁶ are optimized to allow unfolding at low forces, thereby detecting force levels without impairing force transmission (which may be mediated by other molecules such as α -actinin²⁷).

An open question arising from our work is how vinculin binding to talin leads to adhesion growth and YAP translocation. The mechanisms involved are likely to include talin-induced integrin clustering^{34–36}, signalling triggered by vinculin activation on talin binding³⁷, vinculin–actin binding to reinforce the mechanical clutch^{29,38}, and the relay of mechanical forces to the nucleus through stress fibres^{39,40}. Nevertheless and independently of downstream events, our study clarifies how rigidity regulates force transmission, and how force transmission is in turn converted into a biochemical signal. Given the myriad physiological and pathological processes associated with tissue stiffening⁴¹ and YAP signalling⁴², this understanding may also open the door to further fundamental discoveries in biology, and new therapeutic strategies. □

METHODS

Methods and any associated references are available in the online version of the paper.

Note: Supplementary Information is available in the online version of the paper

ACKNOWLEDGEMENTS

We acknowledge support from the Spanish Ministry for Economy and Competitiveness (BFU2011-23111, BFU2012-38146 and BFU2014-52586-REDT), a Career Integration Grant within the seventh European Community Framework Programme (PCIG10-GA-2011-303848), the European Research Council (Grant Agreements 242993 and 240487), the Generalitat de Catalunya, Fundació La Caixa, Fundació la Marató de TV3 (project 20133330), and the National Institutes of Health (US NIH R01AI044902). A.E.-A., R.O. and C.P.-G. were supported respectively by a Juan de la Cierva Fellowship (Spanish Ministry of Economy and Competitiveness), a FI fellowship (Generalitat de Catalunya), and the fundació 'La Caixa'. We thank R. Sunyer, J. Alcaraz, E. Bazellières, F. Rico, S. Garcia-Manyes, N. Bate, N. Berrow and the members of the P.R.-C. and X.T. laboratories for technical assistance and discussions.

AUTHOR CONTRIBUTIONS

A.E.-A. and P.R.-C. conceived the study, A.E.-A., C.Z., X.T. and P.R.-C. designed the experiments, A.E.-A., R.O., Y.C., A.K., C.P.-G. and N.C. performed the experiments, P.R.-C. carried out the theoretical modelling, and A.E.-A. and P.R.-C. wrote the paper.

COMPETING FINANCIAL INTERESTS

The results have been protected under a patent application.

Published online at <http://dx.doi.org/10.1038/ncb3336>

Reprints and permissions information is available online at www.nature.com/reprints

1. Moore, S. W., Roca-Cusachs, P. & Sheetz, M. P. Stretchy proteins on stretchy substrates: the important elements of integrin-mediated rigidity sensing. *Dev. Cell* **19**, 194–206 (2010).
2. Paszek, M. J. et al. Tensional homeostasis and the malignant phenotype. *Cancer Cell* **8**, 241–254 (2005).
3. Engler, A. J., Sen, S., Sweeney, H. L. & Discher, D. E. Matrix elasticity directs stem cell lineage specification. *Cell* **126**, 677–689 (2006).
4. Chan, C. E. & Odde, D. J. Traction dynamics of filopodia on compliant substrates. *Science* **322**, 1687–1691 (2008).
5. Elosegui-Artola, A. et al. Rigidity sensing and adaptation through regulation of integrin types. *Nat. Mater.* **13**, 631–637 (2014).

6. Case, L. B. & Waterman, C. M. Integration of actin dynamics and cell adhesion by a three-dimensional, mechanosensitive molecular clutch. *Nat. Cell Biol.* **17**, 955–963 (2015).
7. Plotnikov, S. V., Pasapera, A. M., Sabass, B. & Waterman, C. M. Force fluctuations within focal adhesions mediate ECM-rigidity sensing to guide directed cell migration. *Cell* **151**, 1513–1527 (2012).
8. Gupta, M. et al. Adaptive rheology and ordering of cell cytoskeleton govern matrix rigidity sensing. *Nat. Commun.* **6**, 7525 (2015).
9. Oakes, P. W., Banerjee, S., Marchetti, M. C. & Gardel, M. L. Geometry regulates traction stresses in adherent cells. *Biophys. J.* **107**, 825–833 (2014).
10. Dupont, S. et al. Role of YAP/TAZ in mechanotransduction. *Nature* **474**, 179–183 (2011).
11. Ghibaudo, M. et al. Traction forces and rigidity sensing regulate cell functions. *Soft Matter* **4**, 1836–1843 (2008).
12. Schiller, H. B. et al. β_1 - and α -class integrins cooperate to regulate myosin II during rigidity sensing of fibronectin-based microenvironments. *Nat. Cell Biol.* **15**, 625–636 (2013).
13. Ghassemi, S. et al. Cells test substrate rigidity by local contractions on sub-micrometer pillars. *Proc. Natl Acad. Sci. USA* **109**, 5328–5333 (2012).
14. Califano, J. P. & Reinhart-King, C. A. Substrate stiffness and cell area predict cellular traction stresses in single cells and cells in contact. *Cell. Mol. Bioeng.* **3**, 68–75 (2010).
15. Etienne, J. et al. Cells as liquid motors: mechanosensitivity emerges from collective dynamics of actomyosin cortex. *Proc. Natl Acad. Sci. USA* **112**, 2740–2745 (2015).
16. Roca-Cusachs, P., Iskratsch, T. & Sheetz, M. P. Finding the weakest link—exploring integrin-mediated mechanical molecular pathways. *J. Cell Sci.* **125**, 3025–3038 (2012).
17. Schoen, I., Pruitt, B. L. & Vogel, V. The Yin-Yang of rigidity sensing: how forces and mechanical properties regulate the cellular response to materials. *Annu. Rev. Mater. Res.* **43**, 589–618 (2013).
18. Austen, K. et al. Extracellular rigidity sensing by talin isoform-specific mechanical linkages. *Nat. Cell Biol.* **17**, 1597–1606 (2015).
19. Margadant, F. et al. Mechanotransduction *in vivo* by repeated talin stretch-relaxation events depends upon vinculin. *PLoS Biol.* **9**, e1001223 (2011).
20. Roca-Cusachs, P., Gauthier, N. C., del Rio, A. & Sheetz, M. P. Clustering of $\alpha_5\beta_1$ integrins determines adhesion strength whereas α,β , and talin enable mechanotransduction. *Proc. Natl Acad. Sci. USA* **106**, 16245–16250 (2009).
21. Zhang, X. et al. Talin depletion reveals independence of initial cell spreading from integrin activation and traction. *Nat. Cell Biol.* **10**, 1062–1068 (2008).
22. del Rio, A. et al. Stretching single talin rod molecules activates vinculin binding. *Science* **323**, 638–641 (2009).
23. Chen, H., Choudhury, D. M. & Craig, S. W. Coincidence of actin filaments and talin is required to activate vinculin. *J. Biol. Chem.* **281**, 40389–40398 (2006).
24. Wegener, K. L. et al. Structural basis of integrin activation by talin. *Cell* **128**, 171–182 (2007).
25. Yao, M. et al. Mechanical activation of vinculin binding to talin locks talin in an unfolded conformation. *Sci. Rep.* **4**, 4610 (2014).
26. Kong, F., Garcia, A. J., Mould, A. P., Humphries, M. J. & Zhu, C. Demonstration of catch bonds between an integrin and its ligand. *J. Cell Biol.* **185**, 1275–1284 (2009).
27. Roca-Cusachs, P. Integrin-dependent force transmission to the extracellular matrix by α -actinin triggers adhesion maturation. *Proc. Natl Acad. Sci. USA* **110**, E1361–E1370 (2013).
28. Tanentzapf, G. & Brown, N. H. An interaction between integrin and the talin FERM domain mediates integrin activation but not linkage to the cytoskeleton. *Nat. Cell Biol.* **8**, 601–606 (2006).
29. Hirata, H., Tatsumi, H., Lim, C. T. & Sokabe, M. Force-dependent vinculin binding to talin in live cells: a crucial step in anchoring the actin cytoskeleton to focal adhesions. *Am. J. Physiol. Cell Physiol.* **306**, C607–C620 (2014).
30. Cohen, D. M., Kutscher, B., Chen, H., Murphy, D. B. & Craig, S. W. A conformational switch in vinculin drives formation and dynamics of a talin-vinculin complex at focal adhesions. *J. Biol. Chem.* **281**, 16006–16015 (2006).
31. Humphries, J. D. et al. Vinculin controls focal adhesion formation by direct interactions with talin and actin. *J. Cell Biol.* **179**, 1043–1057 (2007).
32. Bangasser, B. L., Rosenfeld, S. S. & Odde, D. J. Determinants of maximal force transmission in a motor-clutch model of cell traction in a compliant microenvironment. *Biophys. J.* **105**, 581–592 (2013).
33. Bangasser, B. L. & Odde, D. J. Master equation-based analysis of a motor-clutch model for cell traction force. *Cell. Mol. Bioeng.* **6**, 449–459 (2013).
34. Saltel, F. et al. New PI(4,5)P2- and membrane proximal integrin-binding motifs in the talin head control $\beta 3$ -integrin clustering. *J. Cell Biol.* **187**, 715–731 (2009).
35. Klapholz, B. et al. Alternative mechanisms for talin to mediate integrin function. *Curr. Biol.* **25**, 847–857 (2015).
36. Iwamoto, D. V. & Calderwood, D. A. Regulation of integrin-mediated adhesions. *Curr. Opin. Cell Biol.* **36**, 41–47 (2015).
37. Case, L. B. et al. Molecular mechanism of vinculin activation and nanoscale spatial organization in focal adhesions. *Nat. Cell Biol.* **17**, 880–892 (2015).
38. Thievessen, I. et al. Vinculin–actin interaction couples actin retrograde flow to focal adhesions, but is dispensable for focal adhesion growth. *J. Cell Biol.* **202**, 163–177 (2013).
39. Roca-Cusachs, P. et al. Micropatterning of single endothelial cell shape reveals a tight coupling between nuclear volume in G1 and proliferation. *Biophys. J.* **94**, 4984–4995 (2008).
40. Swift, J. et al. Nuclear lamin-A scales with tissue stiffness and enhances matrix-directed differentiation. *Science* **341**, 1240104 (2013).
41. DuFort, C. C., Paszek, M. J. & Weaver, V. M. Balancing forces: architectural control of mechanotransduction. *Nat. Rev. Mol. Cell Biol.* **12**, 308–319 (2011).
42. Plouffe, S. W., Hong, A. W. & Guan, K. L. Disease implications of the Hippo/YAP pathway. *Trends Mol. Med.* **21**, 212–222 (2015).

METHODS

Cell culture constructs, and transfection. Talin 1^{-/-} mouse embryonic fibroblasts were described previously^{20,21}, and cultured in DMEM 1× (Life Technologies, 41965), supplemented with 15% FBS. Wild-type mouse embryonic fibroblasts were also described previously²⁰, and cultured in DMEM supplemented with 10% FBS. All cells tested negative for mycoplasma contamination. All transfections were carried out using the Neon transfection device according to the manufacturer's instructions. To deplete talin levels, cells were transfected with talin 2 shRNA, which contained puromycin resistance (previously described²¹). One day after transfection, cells were incubated with 2 µg ml⁻¹ puromycin for four days to select for transfected cells. Resulting transfection efficiency was of 52%, with a standard deviation of 11% (see Supplementary Fig. 3). EGFP-talin 1 was a gift from D. Critchley (University of Leicester, UK) and described previously⁴³, EGFP-talin 1 IVVI was prepared in-house from EGFP-talin 1 by introducing four point mutations (T8091/T833V/T867V/T901I). EGFP-talin 1 head (Addgene plasmid no. 32856) and EGFP-talin 1 rod (Addgene plasmid no. 32855) were obtained from A. Huttenlocher (University of Wisconsin-Madison, USA)⁴⁴. EGFP-VD1 (Addgene plasmid no. 46270, described as pEGFPC1/GgVcl 1-258) and EGFP-VD1 A50I (Addgene plasmid no. 46271, described as pEGFPC1/GgVcl 1-258 A50I) were obtained from S. Craig (Johns Hopkins School of Medicine, USA)³⁰. EGFP-FL talin 1 W359A and EGFP-talin 1 L325R (both FL and head fragment) were gifts from M. Ginsberg's laboratory (UC San Diego, USA) and described previously²⁴. Lifeact-GFP was described previously⁵. For talin 2 shRNA experiments, cells were transfected with talin 2 shRNA+corresponding plasmid five days before experiments. For control cells, transfections were made the day before experiments.

Antibodies and chemicals. To block integrin function, we used an inhibitory antibody against α_vβ₁ (10 µg ml⁻¹, clone BMB5 produced in rat, Millipore) and a GPen-GRGDSPCA peptide (called GPen throughout the text) specifically recognizing α_vβ₃ integrin^{20,45} (Bachem). Blebbistatin was from CalBiochem. Antibodies used for immunostaining were a β₃ monoclonal antibody recognizing the ligand-bound integrin (clone LIBS1, 1:500 dilution) kindly provided by M. Ginsberg's laboratory⁴⁶, a vinculin monoclonal antibody (clone h-Vin1 produced in mouse, Sigma catalogue no. V9264, 1:500 dilution), and a rabbit polyclonal antibody recognizing focal adhesion kinase phosphorylated at Tyr397 (Thermofisher catalogue no. 44-624G, 1:150 dilution). For YAP measurements, we used Hoechst 33342 (Invitrogen) to stain the nucleus and a YAP monoclonal antibody (clone 63.7 produced in mouse, Santa Cruz catalogue no. sc-101199, 1:200 dilution). Phalloidin-tetramethylrhodamine B isothiocyanate (Sigma) was used to label actin. For western blots, we used a talin monoclonal antibody (clone 8d4 produced in mouse, Sigma catalogue no. T3287, 1:1,000 dilution), a myosin light chain polyclonal antibody produced in rabbit (Cell Signaling catalogue no. 3672, 1:200 dilution), a phospho-myosin light chain polyclonal antibody produced in rabbit (Cell Signaling catalogue no. 3674, 1:500 dilution) and a GAPDH monoclonal antibody (clone 6C5 produced in mouse, Santa Cruz catalogue no. sc-32233, 1:1,000 dilution).

Preparation of polyacrylamide gels. Polyacrylamide gels were prepared as previously described⁵. Briefly, glass-bottom dishes (Mattek) were activated with a solution of 3-(trimethoxysilyl)propyl methacrylate (Sigma), acetic acid and ethanol (1:1:14), washed three times with ethanol and air-dried for 10 min. To generate gels of different stiffness, different concentrations of acrylamide and bis-acrylamide were mixed (see Supplementary Table 2) in a solution containing 0.5% ammonium persulfate, 0.05% tetramethylethylenediamine (Sigma), 0.4% fluorescent red carboxylated nanobeads (Invitrogen), and 4.8 mg ml⁻¹ NH-acrylate. Ten microlitres of this solution was then placed on the centre of glass-bottom dishes and covered with 12-mm-diameter glass coverslips. After gel polymerization, top coverslips were removed and gels were incubated with fibronectin (Sigma) overnight at 4 °C. After washing gels with PBS, cells were then trypsinized and plated on gels. Experiments were carried out 4–8 h after cell seeding. To compare fibronectin coating densities on the gels, fibronectin used for coating was previously labelled with an Alexa Fluor 488 protein labelling kit according to the manufacturer's instructions (A-10235, Thermo Fisher Scientific). Then, fibronectin coating densities at the gel surface were measured by acquiring epifluorescence images with a 20× objective (NA 0.45), and quantifying resulting fluorescence intensity levels.

Polyacrylamide gel stiffness measurements. The stiffness (Young's modulus) of polyacrylamide gels was measured by atomic force microscopy as previously described⁴⁷. Briefly, measurements were made with a custom-built atomic force microscope attached to an inverted optical microscope (Nikon TE200). Silicon nitride pyramidal tips with an effective half-angle θ of 20° and a nominal spring constant of $k = 0.01\text{--}0.03 \text{ N m}^{-1}$ were used (MLCT, Bruker). The actual spring constant was calibrated by thermal tuning using the simple harmonic oscillator model⁴⁸. The Young's modulus was measured by recording 10 force-displacement curves with a peak-to-peak amplitude of 6 µm and a frequency of 1 Hz. Three points near the gel

centre were selected in each gel, separated 5 µm from each other. For each stiffness, ≥6 gels produced in two batches were measured. To compute the Young's modulus (E), the Hertz model equation for pyramidal tips was fitted to the force-displacement curves. The equation was fitted for an effective indentation of 1,000 nm.

Traction force measurements. Traction force measurements were performed as described previously⁵. Briefly, cells seeded on gels were placed on an inverted microscope (Nikon Eclipse Ti). Phase contrast images of single cells and fluorescence images of the embedded nanobeads were obtained with a 40× objective (NA 0.6). At the end of the measurements, cells were trypsinized and an image of bead position in the relaxed state of the gel was acquired. By comparing bead positions with and without cells, a map of gel deformations caused by cells was first obtained using custom particle imaging velocimetry software⁴⁹. Then, after assuming that gel displacements were caused by forces exerted by cells in the cell-gel contact area, the corresponding map of cell forces was calculated using a previously described Fourier transform algorithm^{39,50}. The average forces per unit area exerted by each cell were then calculated. To calculate the minimum detectable force levels for each rigidity, we followed the same procedure in cell-free gel areas, and calculated the resulting forces. Phase contrast images were also used to calculate average cell spreading areas as a function of substrate stiffness.

Immunostaining. For fluorescence staining, cells were fixed with 4% paraformaldehyde, permeabilized with 0.1% Triton X-100, and labelled first with primary antibodies (1 h, room temperature), and then with Alexa-conjugated secondary antibodies (Invitrogen; 1 h, room temperature). Phalloidin was added with the secondary antibody. Fluorescence images were then acquired with a 60× oil-immersion objective (NA 1.40) using a spinning-disc confocal microscope (Andor). The length of adhesions was assessed by measuring the length of bright vinculin, β₃ integrin or pFAK stainings at the cell edge. Integrin density was assessed as described previously⁵. The area containing pFAK-positive adhesions was calculated after segmenting adhesions as previously described⁵¹. The degree of YAP nuclear localization was assessed by calculating the ratio between YAP fluorescence in the nuclear region and the cytoplasmic region immediately adjacent. Nuclear and cytoplasmic regions were previously determined by co-staining the nucleus with Hoechst 33342.

Rearward flow measurements. To measure actin rearward flow, cells were transfected with Lifeact-GFP. Cells were then plated on gels of varying rigidity, and imaged every second for 2 min with a 60× oil-immersion objective (NA 1.40) with a spinning-disc confocal microscope (Andor). For each cell, kymographs were obtained at the cell periphery, and actin speed was measured from the slope of actin features observed in the kymographs. In cells plated on 0.6 kPa gels, actin features were so diffuse that no reliable slopes could be measured in kymographs.

Western blots. For western blotting of talin, myosin light chain, and phosphorylated myosin light chain, cells were directly incubated with 1× Laemli and boiled at 95 °C for 5 min. Cell lysates were loaded on 4–20% polyacrylamide gels (Bio-Rad), and electrophoresis proteins were then transferred to a nitrocellulose membrane (Whatman, GE Healthcare Life Sciences), which was blocked with 5% dry-milk-Tris buffer saline-0.2% Tween. The membrane was incubated first with primary antibodies (overnight, 4 °C), and then with horseradish-peroxidase-coupled secondary antibodies (1 h, room temperature). Bands were revealed using the LumiLight kit (Roche) and quantified using ImageJ software.

Single fibronectin-α_vβ₃ bond lifetime measurements. The lifetime of single fibronectin-α_vβ₃ bonds was measured using a previously described biomembrane force probe (BFP) technique⁵². Biotinylated red blood cells (RBCs) for BFP experiments were collected abiding a Georgia Institute of Technology IRB-approved protocol, and prepared as previously described⁵². Target beads were first covalently linked with anti-Penta His (histidine) antibody (catalogue no. 34660, Qiagen), and then further covered with Hexa-His tagged recombinant α_vβ₃ ectodomain, which was a gift from J. Takagi, Osaka University, Japan⁵³. Probe beads were first functionalized with streptavidin through covalent linkage and then partially covered with biotinylated fibronectin module III, domain 7–10 (FN_{III7-10}, a generous gift from A. Garcia, Georgia Tech, USA). To provide maximum integrin activation, experiments were carried out in the presence of 2 mM Mn²⁺. In a BFP experiment, the probe bead was glued through biotin-streptavidin interaction onto the apex of the RBC, which was aspirated by a micropipette and acted as a force transducer. A second opposing micropipette grabbed the target bead and drove it to repeatedly impinge the probe bead, contact for 2 s and then retract (ramping). Displacement of the probe bead was tracked in real time, which reflected the force exerted on it. If an adhesion event occurred, meaning that one bond or more was formed between the two bead surfaces, ramping resulted in a tensile force signal of the probe bead that pulled on and elongated the RBC. The ramping was then paused at a preset force level (clamping) to wait for bond dissociation, manifested by a

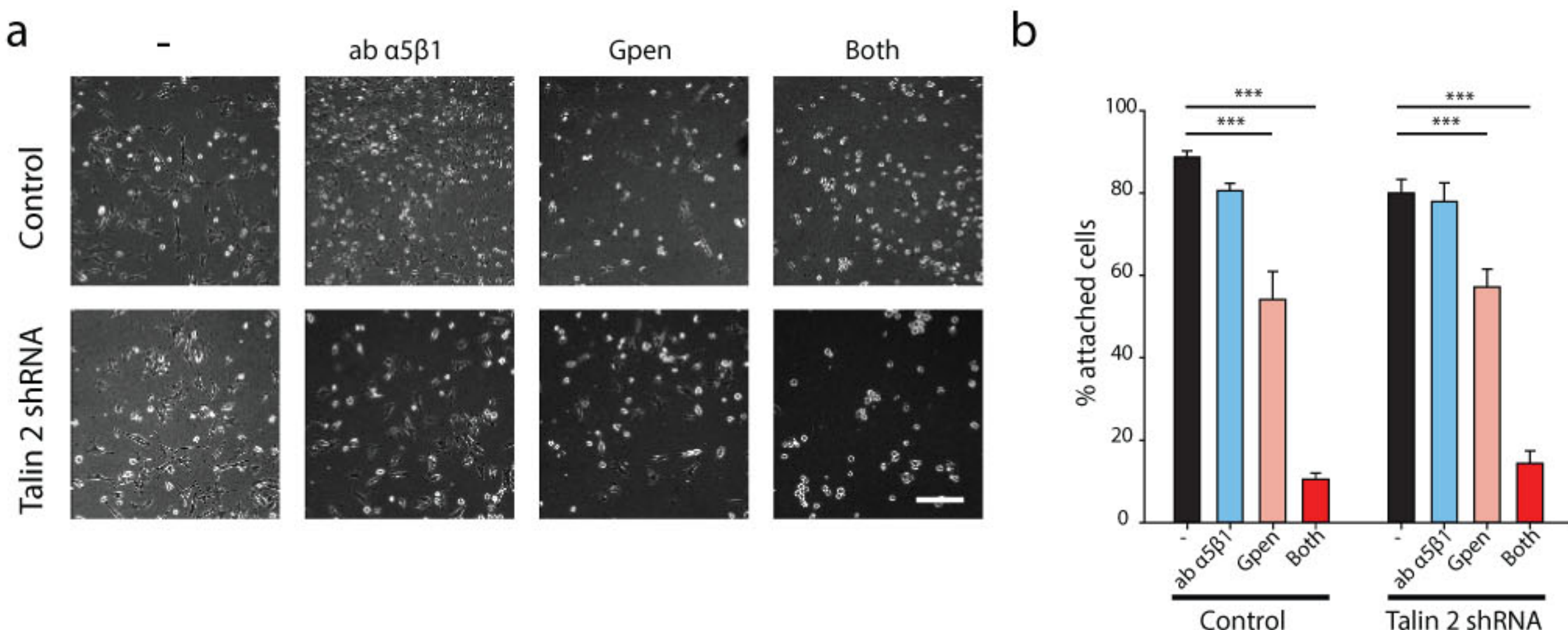
backward deformation of the RBC and a sudden force drop to 0 pN. To ensure that most adhesion events (>90%) were single molecular interactions, the frequency of adhesion occurrence was adjusted to be low (<20%) by titrating the coating densities on both beads⁵⁴. The time that each adhesion survived during clamping is termed the lifetime, which was collected under a range of positive forces. To derive lifetimes under zero force, the ramping was paused at 0 pN and held for 20 s. Sudden drops/increases in the thermal fluctuation signal of the probe bead were used to judge the bond association/dissociation, given that bonding suppresses thermal fluctuation⁵⁵. The average lifetimes were then plotted against the corresponding forces to form a ‘lifetime versus force’ curve⁵⁶. To confirm binding specificity, control experiments were performed by either adding a $\alpha_v\beta_3$ blocking antibody (clone LM609, EMD Millipore) or coating beads only with streptavidin instead of FN_{III7-10}. Both controls yielded rare binding (~3%).

Statistics and reproducibility. In all figures, measurements are reported as mean \pm standard error of the mean (s.e.m.). Statistical comparisons were carried out with two-tailed Student’s *t*-tests when two cases were compared and with analysis of variance (ANOVA) tests when more cases were analysed. The results of all experiments were reproducible; the number of independent reproductions for each experiment is specified in the figure legends.

Computational model and code availability. Details on the computational model and its implementation are provided in the Supplementary Note. Matlab code employed to generate the model is available on request to rocacusachs@ub.edu.

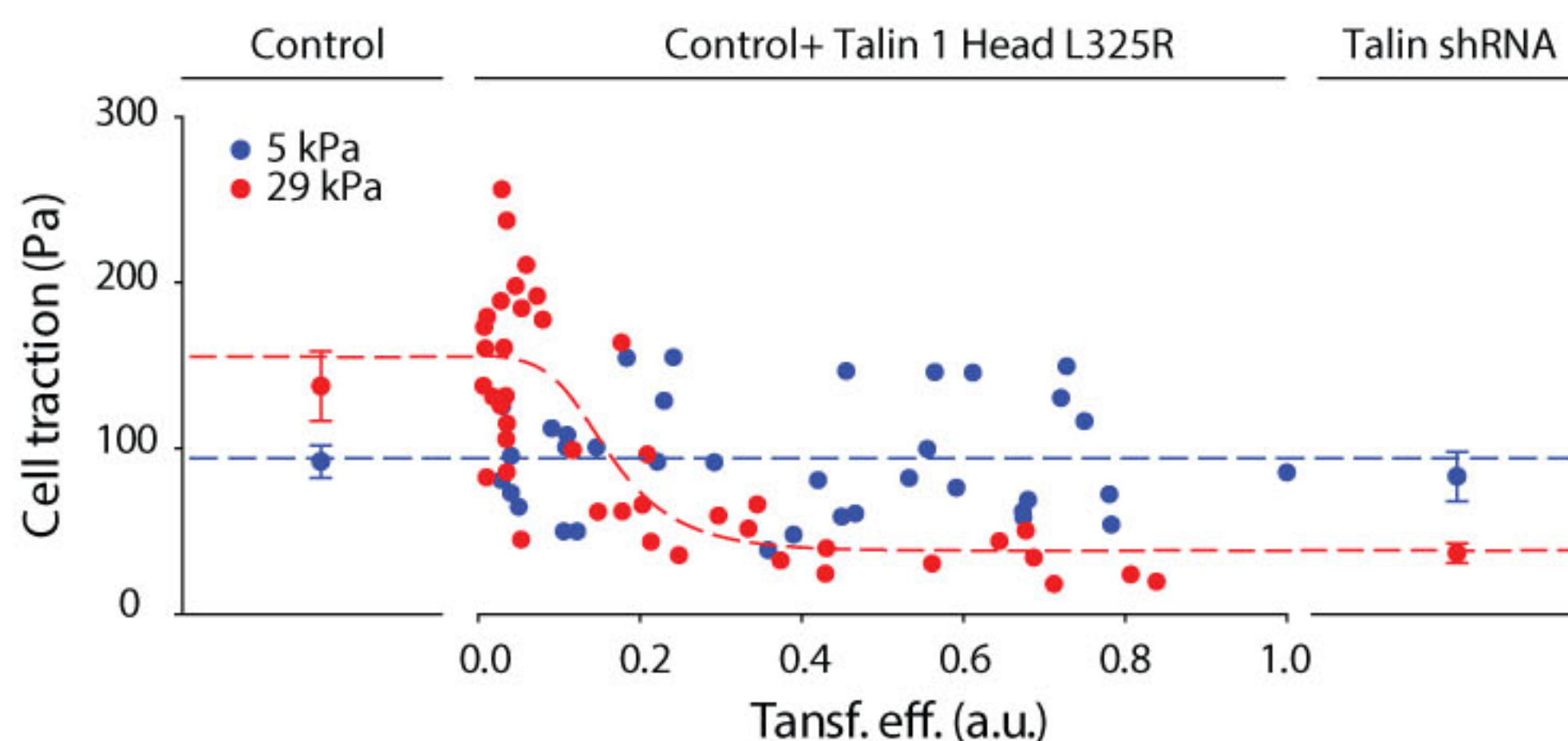
43. Bate, N. *et al.* Talin contains a C-terminal calpain2 cleavage site important in focal adhesion dynamics. *PLoS ONE* **7**, e34461 (2012).
44. Simonson, W. T., Franco, S. J. & Huttenlocher, A. Talin1 regulates TCR-mediated LFA-1 function. *J. Immunol.* **177**, 7707–7714 (2006).

45. Pierschbacher, M. D. & Ruoslahti, E. Influence of stereochemistry of the sequence Arg-Gly-Asp-Xaa on binding-specificity in cell-adhesion. *J. Biol. Chem.* **262**, 17294–17298 (1987).
46. Frelinger, A. L. 3rd, Du, X. P., Plow, E. F. & Ginsberg, M. H. Monoclonal antibodies to ligand-occupied conformers of integrin α IIb β 3 (glycoprotein IIb-IIIa) alter receptor affinity, specificity, and function. *J. Biol. Chem.* **266**, 17106–17111 (1991).
47. Alcaraz, J. *et al.* Microrheology of human lung epithelial cells measured by atomic force microscopy. *Biophys. J.* **84**, 2071–2079 (2003).
48. Hutter, J. L. & Bechhoefer, J. Calibration of atomic-force microscope tips. *Rev. Sci. Instrum.* **64**, 1868–1873 (1993).
49. Serra-Picamal, X. *et al.* Mechanical waves during tissue expansion. *Nat. Phys.* **8**, U628–U666 (2012).
50. Butler, J. P., Tolic-Norrelykke, I. M., Fabry, B. & Fredberg, J. J. Traction fields, moments, and strain energy that cells exert on their surroundings. *Am. J. Physiol. Cell Physiol.* **282**, C595–C605 (2002).
51. Elosegui-Artola, A. *et al.* Image analysis for the quantitative comparison of stress fibers and focal adhesions. *PLoS ONE* **9**, e107393 (2014).
52. Chen, Y. *et al.* Fluorescence biomembrane force probe: concurrent quantitation of receptor-ligand kinetics and binding-induced intracellular signaling on a single cell. *J. Vis. Exp.* **102**, e52975 (2015).
53. Takagi, J., Petre, B. M., Walz, T. & Springer, T. A. Global conformational rearrangements in integrin extracellular domains in outside-in and inside-out signaling. *Cell* **110**, 599–611 (2002).
54. Chesla, S. E., Selvaraj, P. & Zhu, C. Measuring two-dimensional receptor-ligand binding kinetics by micropipette. *Biophys. J.* **75**, 1553–1572 (1998).
55. Chen, W., Zarnitsyna, V. I., Sarangapani, K. K., Huang, J. & Zhu, C. Measuring receptor-ligand binding kinetics on cell surfaces: from adhesion frequency to thermal fluctuation methods. *Cell. Mol. Bioeng.* **1**, 276–288 (2008).
56. Chen, W., Lou, J. & Zhu, C. Forcing switch from short- to intermediate- and long-lived states of the α A domain generates LFA-1/ICAM-1 catch bonds. *J. Biol. Chem.* **285**, 35967–35978 (2010).



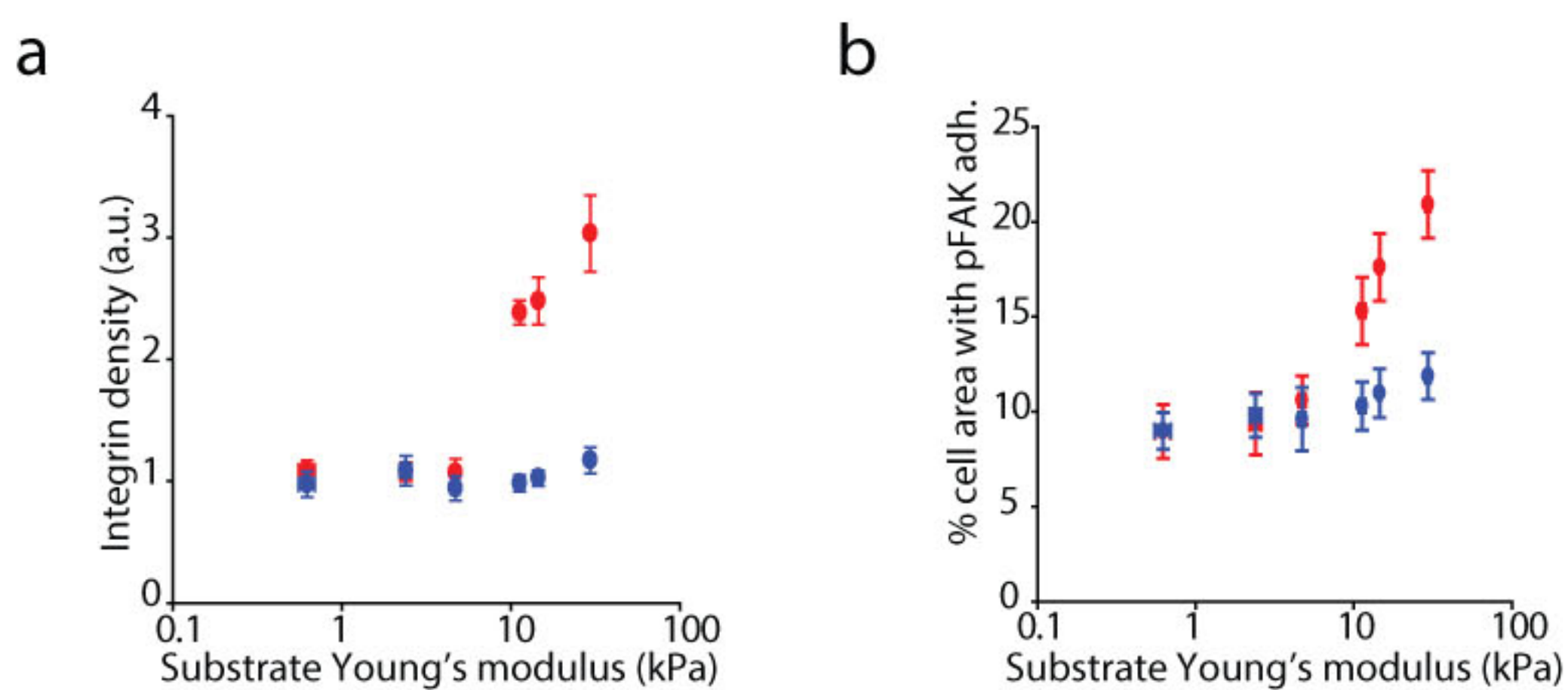
Supplementary Figure 1 Cell adhesion to fibronectin-coated gels is mediated by $\alpha v\beta 3$ and $\alpha 5\beta 1$ integrins. **a**, Images showing control and Talin 2 shRNA cells on 29 kPa fibronectin-coated polyacrylamide gels with or without blocking integrin $\alpha 5\beta 1$ (using 10 μ g/ml of BMB5 antibody), $\alpha v\beta 3$ (using 0.5 mM of the specific Gopen peptide) or both.

Scale bar is 50 μ m. **b**, Corresponding quantification of the percentage of spread cells (from left to right, n = 12, 12, 11, 11, 20, 11, 10, 12 fields of view)(***, p ≤ 0.001, two-way Anova). Data show 1 out of 2 independent experiments. Blocking both integrins abolished cell adhesion almost completely.



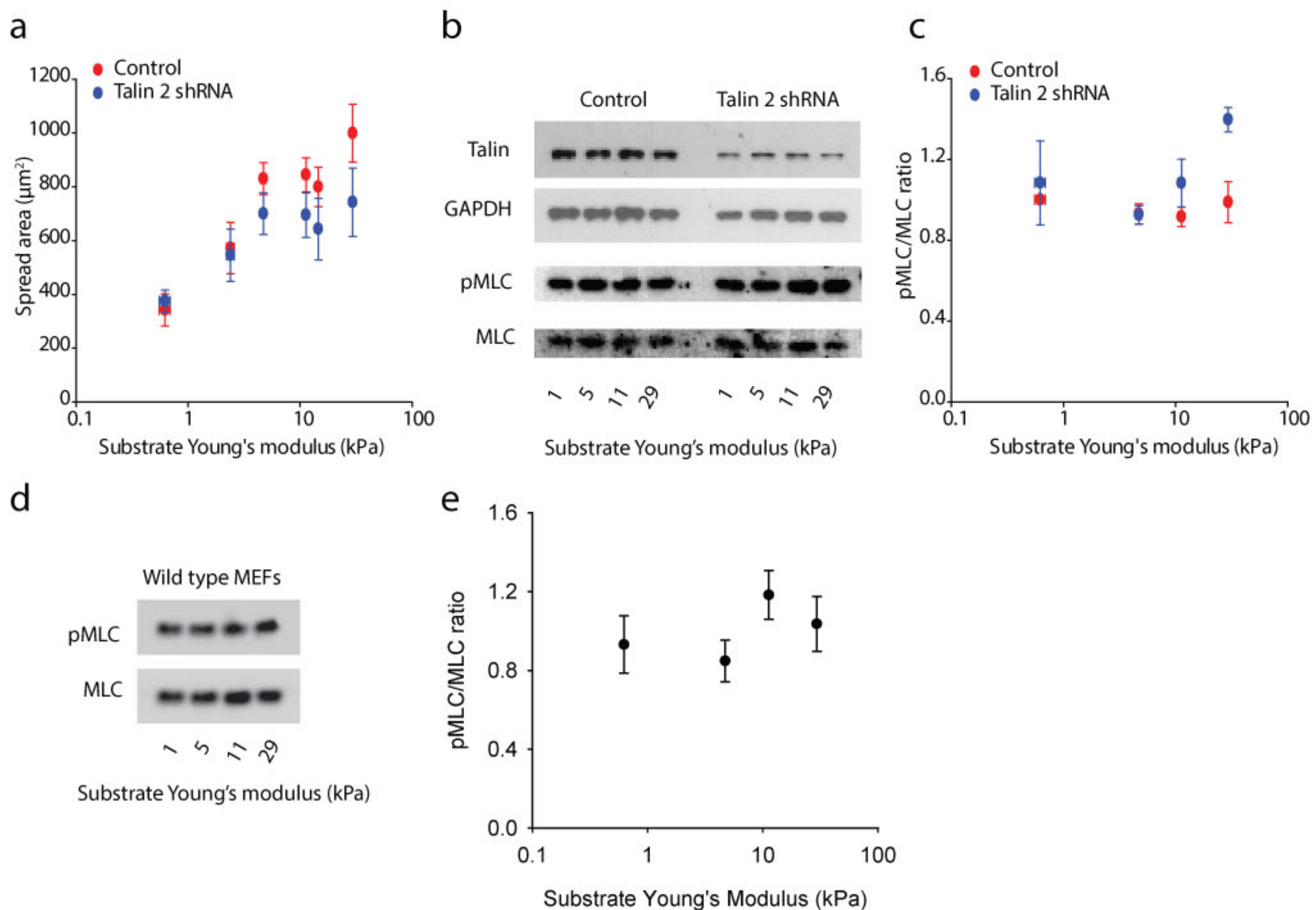
Supplementary Figure 2 Talin1 Head L325R expression progressively reduces force transmission above but not below the rigidity threshold. Traction forces exerted by control cells on 5 kPa gels (blue) and 29 kPa gels (red) as a function of the efficiency of transfection with Talin1 Head L325R. Values are compared to mean forces of untransfected control cells (left) and talin

shRNA cells (right). Note that in figure 1, talin 1 Head L325R data represent averages for well transfected cells only. Dotted lines represent sigmoidal fits to the data. (Control: 5kPa, n=35 cells; 29 kPa, n= 12 cells. Control + Talin 1 Head: 5 kPa, n=37 cells; 29 kPa, n=42 cells. Talin 2 shRNA: 5 kPa, n=34 cells; 29 kPa, n= 29 cells). Data show 1 out of 3 independent experiments.



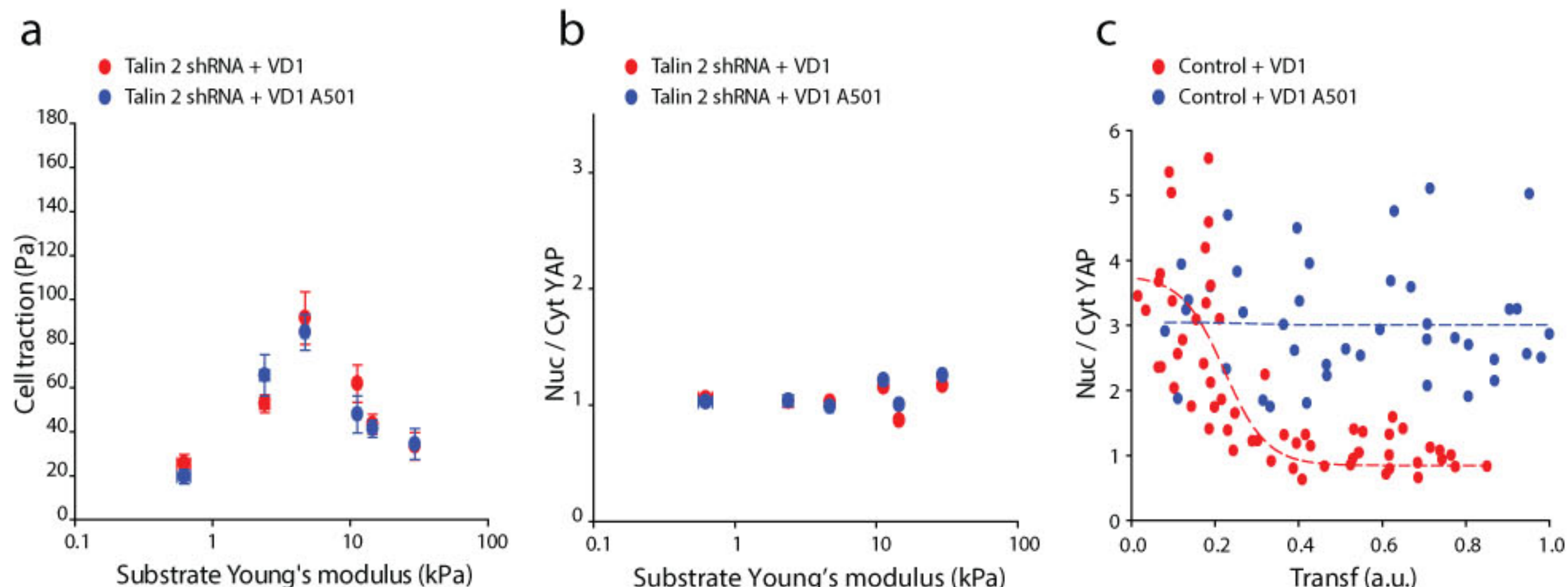
Supplementary Figure 3 Further quantifications of integrin and pFAK in adhesions. **a**, quantification of integrin density from staining images of ligand bound $\beta 3$ for Control cells (red, n=20, 31, 24, 33, 20, 29 fields respectively for increasing rigidity measured in 8-10 cells) and Talin 2 shRNA cells (blue, n= 20, 21, 25, 29, 24, 29 fields measured in 8-9 cells). Data show 1 out of 3 independent experiments. Integrin densities were significantly different between control and depleted cells only above

5 kPa ($p<0.001$, two-way Anova). **b**, Quantification of the percentage of cell spreading area covered by pFAK-positive adhesions from staining images of Control cells (red, n= 11, 10, 17, 17, 17, 15 cells respectively for increasing rigidity) and Talin 2 shRNA cells (blue, n= 11, 10, 10, 12, 10, 10 cells) as a function of substrate stiffness. Data show 1 out of 3 independent experiments. Significant differences were observed only above 5 kPa ($p=0.039$, two-way Anova).



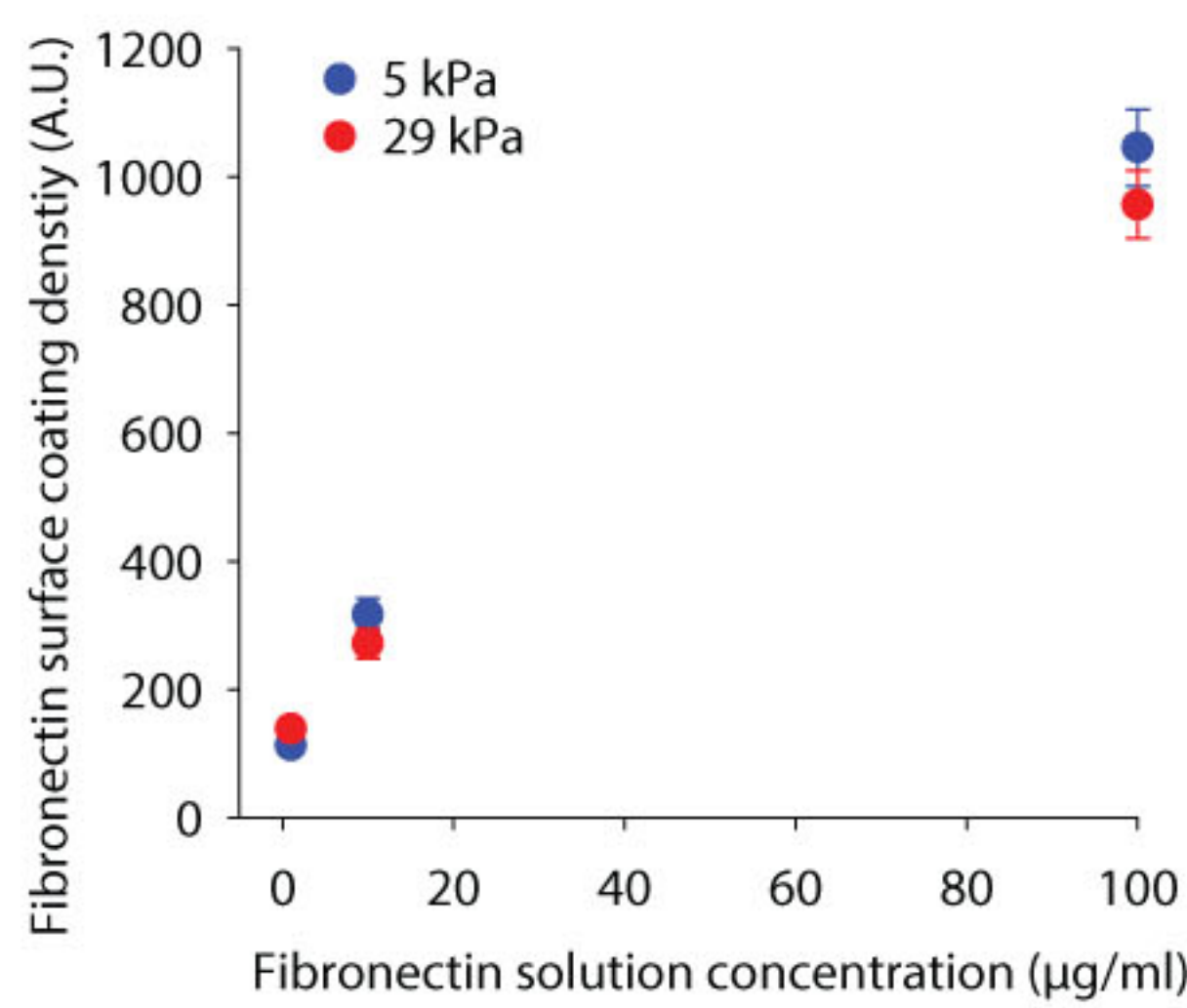
Supplementary Figure 4 Dependence of cell area and myosin phosphorylation on substrate stiffness. **a**, Quantification of cell area in response to substrate stiffness for control and talin 2 shRNA cells (Control: n = 17, 12, 35, 42, 42, 12 cells respectively for increasing stiffness; Talin 2 shRNA: n = 10, 11, 34, 23, 25, 29 cells). Data show 1 out of 14 independent experiments. Talin depletion did not have a significant effect (two-way Anova). **b**, For cells plated on gels of the indicated stiffness, representative western blots of talin, GAPDH as loading control, phosphorylated myosin light chain and total myosin light chain for

Control and Talin 2 shRNA cells. **c**, Corresponding quantification of the phosphorylated/total myosin light chain ratio (pooled from n = 3 independent experiments). No significant differences were found (two-way Anova). **d**, Representative western blots of phosphorylated myosin light chain and total myosin light chain for wild-type MEF cells. **e**, Corresponding quantification of the phosphorylated/total myosin light chain ratio (pooled from n = 3 independent experiments). No significant differences were found, suggesting that myosin phosphorylation is not significantly affected in MEF cells regardless of talin (one-way Anova).

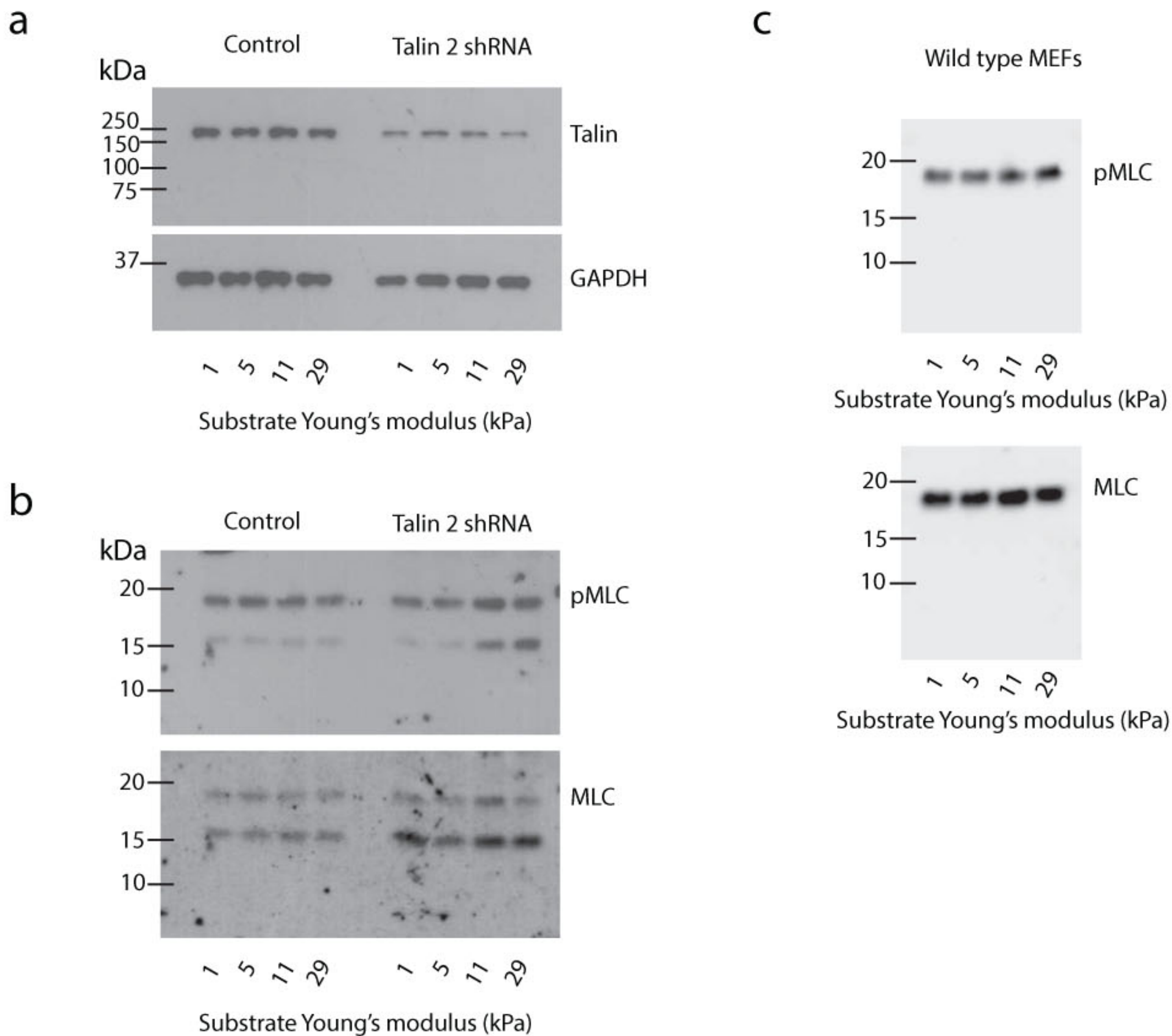


Supplementary Figure 5 Further analyses on the effects of vinculin fragments. **a**, Average forces in response to substrate stiffness for cells transfected with Talin 2 shRNA + VD1 (red, n=10, 13, 11, 11, 13, 10 cells, respectively for increasing stiffness) and Talin 2 shRNA + VD1 A501 (blue, n=11, 11, 12, 11, 11, 10 cells). No significant differences were found between transfections (two-way Anova). Data show 1 out of 3 independent experiments. **b**, Quantification of Nuclear/Cytosolic YAP ratio for the same conditions as in (a) (Talin 2 shRNA + VD1: n=26, 20, 30, 29, 32, 32 cells respectively for increasing stiffness; Talin 2 shRNA + VD1 A501: n=22, 21, 21, 23, 23, 24 cells). No significant differences were found between transfections (two-way

Anova). Data show 1 out of 3 independent experiments. **c**, Quantification of Nuclear/Cytosolic YAP ratio for control cells transfected with VD1 (red) and or VD1 A501 (blue) as a function of transfection efficiency (measured as the relative intensity of EGFP fluorescence) on 29 kPa polyacrylamide gels (Control + VD1: n=59 cells; Control + VD1 A501: n=49 cells). Data show 1 out of 3 independent experiments. Dashed lines are a sigmoidal fit to the experimental results for each condition. Further confirming the blocking role of VD1, increasing transfection efficiencies progressively decreased nuclear localization of YAP. In contrast, increasing efficiencies of transfection with VD1 A501 had no effect.



Supplementary Figure 6 Fibronectin coating densities. Resulting fibronectin coating densities on the surface of polyacrylamide gels of 5 and 29 kPa coated with solutions containing 1, 10, or 100 $\mu\text{g}/\text{ml}$ of fibronectin. $n=6$ gels in all cases except 100 $\mu\text{g}/\text{ml}$ -29 kPa (5 gels). Data pooled from two independent experiments.



Supplementary Figure 7 Unprocessed versions of the western blots shown in supplementary fig. 4. **a,b**, blots corresponding to panel b in supplementary fig. 4. All measured bands corresponded to the molecular weights of the different

proteins as detailed by antibody providers: talin (225-235 kDa), GAPDH (36 kDa), and MLC (18 kDa). Note that blots do not show the entire molecular weight spectrum because membranes were cut before antibody incubation to incubate each band only with the relevant antibody.

Parameter	meaning	Value	Origin	Sensitivity	95% Confidence intervals
n_f	Number of FN molecules	1200	Adjusted	1.66	940 – 1460
K_{onf}	True binding rate	$2.11 \times 10^{-4} \text{ } \mu\text{m}^2/\text{s}$	Adjusted, of the order of values reported for $\alpha\text{II}\beta\beta 3^1$	1.49	$1.8 - 2.4 \times 10^{-4} \text{ } \mu\text{m}^2/\text{s}$
n_m	Number of myosin motors	800	Adjusted	-1.16	730 – 870
d_{add}	Integrins added after each reinforcement event	$24 \text{ } / \mu\text{m}^2$	Adjusted	-0.83	$17 - 31 \text{ } / \mu\text{m}^2$
FR	Fraction of force experienced by talin	0.073	Adjusted	-0.95	0.068 – 0.078
F_m	Myosin motor stall force	2 pN	²		
v_u	Unloaded myosin motor velocity	110 nm/s	Values measured here and ³		
d_{int}	Integrin density on the membrane	$300 \text{ } / \mu\text{m}^2$	Set, of the order of reported values ⁴		
K_{off}	Integrin unbinding rate	Catch bond	Measured ($\alpha\text{v}\beta 3$) and ⁵ ($\alpha 5\beta 1$)		
K_{fold}	Talin unfolding rate	Slip bond	⁶		
K_{unfold}	Talin refolding rate	Slip bond	⁶		
k_c	Clutch spring constant	1 nN/nm	⁷		
r_a	Radius of adhesion	1700 nm	Set		

Supplementary Table 1 Model parameters. These parameters correspond to the reference case (control cells, no treatment, 10 $\mu\text{g}/\text{ml}$ fibronectin coating). Other cases were fitted by modifying only the relevant parameters to the applied treatment (see legend of Fig. 6 for parameter values). The parameters employed to adjust the model to the different experimental conditions are listed as “adjusted”. For those parameters, sensitivity values report how the threshold rigidity for talin unfolding depends on changes in the parameter (see methods for details). Positive/negative values indicate that the threshold rigidity increases/decreases as the parameter increases.

SUPPLEMENTARY INFORMATION

% Acrylamide	% Bis-acrylamide	Young's modulus (kPa) (Mean \pm S.E.)	Number of gels measured
4	0.03	0.62 \pm 0.07	11
5.5	0.044	2.39 \pm 0.13	9
7.46	0.044	4.71 \pm 0.22	12
7.49	0.10	11.29 \pm 0.49	9
7.52	0.16	14.54 \pm 0.24	6
12	0.15	29.45 \pm 0.10	6

Supplementary Table 2 Polyacrylamide gel rigidities measured with AFM. Data shown were pooled from the number of independent gel measurements indicated.

Figure panel	n value	# of independent experiments	Statistical significance
6a	Control: n=16, 17, 39, 17, 11, 21 cells Talin 2 shRNA: n=10, 11, 20, 21, 25, 29 cells	3	p=0.014 between Control and Talin 2 shRNA only above 2 kPa
6b	Control: n=11, 19, 10, 10, 10, 12 cells Talin 2 shRNA: n=10, 11, 10, 12, 10, 10 cells	3	p=0.039 between Control and Talin 2 shRNA only above 5 kPa
6c	Control: n=10, 16, 13, 28, 14, 28 cells Talin 2 shRNA: n=10, 10, 14, 32, 11, 12 cells	3	p=0.022 between Control and Talin 2 shRNA only above 11 kPa
6d	Control: n= 17, 12, 35, 42, 42, 12 cells Talin shRNA: n= 10, 11, 34, 23, 25, 29 cells .	14	P=0.006 between Control and Talin 2 shRNA only above 5 kPa
6e	Control: n= 17, 13, 14, 12, 11, 12 cells Talin shRNA: n= 10, 11, 11, 11, 11, 13 cells .	3	p<0.001 between Control and Talin 2 shRNA only above 5 kPa
6f	Control: n= 12, 12, 21, 32, 37, 17 cells Talin shRNA: n= 13, 14, 21, 15, 22, 14 cells .	3	p<0.001 between Control and Talin 2 shRNA only at 29 kPa
6g	Control: n= 12, 12, 12, 56, 33, 21 cells Talin shRNA: n= 14, 13, 15, 46, 17, 28 cells .	3	p=0.003 between Control and Talin 2 shRNA only above 11 kPa
6h	Control: n= 16, 27, 11, 18, 15, 15 cells Talin shRNA: n= 13, 14, 11, 15, 14, 15 cells .	3	p<0.001 between Control and Talin 2 shRNA only above 5 kPa
6i	Control: n= 11, 10, 14, 11, 14, 10 cells Talin shRNA: n= 11, 10, 12, 10, 15, 11 cells . 1µg/ml, n=22, 27, 29, 55, 33, 25 cells	3	No statistical differences For 5 kPa, p=0.033 between 1µg/ml and 10 µg/ml and p=0.033 between 1µg/ml and 100 µg/ml.
6j	10 µg/ml, n=20, 22, 21, 29, 20, 39 cells 100 µg/ml, n= 25, 41, 40, 57, 27, 24 cells 0.05 mM, n=22, 21, 23, 29, 21, 30 cells	3	For 11 kPa, p<0.001 between 100µg/ml and, both, 1 µg/ml and 10 µg/ml.
6k	0.15 mM, n=21, 23, 21, 21, 26, 35 cells 0.5 mM, n= 23, 20, 20, 22, 20, 26 cells 5 µM, n=21, 25, 36, 27, 45, 59 cells	3	No statistical differences
6l	15 µM, n=25, 26, 29, 27, 105, 23 cells 50 µM, n= 21, 24, 32, 42, 28, 21 cells	3	p<0.001 between 5µM and both 15 µM and 50 µM above 11 kPa

Supplementary Table 3 Statistical details of figure 6 panels. All statistical comparisons were carried out using 2-way Anova. All n values are reported sequentially for increasing stiffness. All data shown represent 1 experiment out of the number of independent experiments specified in the table.

SUPPLEMENTARY INFORMATION

References to Supplementary Table 1

1. Litvinov, R.I. *et al.* Resolving two-dimensional kinetics of the integrin alpha1beta1beta3-fibrinogen interactions using binding-unbinding correlation spectroscopy. *J. Biol. Chem.* **287**, 35275–35285 (2012).
2. Molloy, J.E., Burns, J.E., Kendrick-Jones, J., Tregear, R.T. & White, D.C. Movement and force produced by a single myosin head. *Nature* **378**, 209–212 (1995).
3. Chan, C.E. & Odde, D.J. Traction dynamics of filopodia on compliant substrates. *Science* **322**, 1687–1691 (2008).
4. Elosegui-Artola, A. *et al.* Rigidity sensing and adaptation through regulation of integrin types. *Nat. Mater.* **13**, 631–637 (2014).
5. Kong, F., Garcia, A.J., Mould, A.P., Humphries, M.J. & Zhu, C. Demonstration of catch bonds between an integrin and its ligand. *J. Cell Biol.* **185**, 1275–1284 (2009).
6. Yao, M. *et al.* Mechanical activation of vinculin binding to talin locks talin in an unfolded conformation. *Scientific reports* **4**, 4610 (2014).
7. Roca-Cusachs, P., Iskratsch, T. & Sheetz, M.P. Finding the weakest link - exploring integrin-mediated mechanical molecular pathways. *J. Cell Sci.* **125**, 3025–3038 (2012).

Supplementary Video Legends

Supplementary Video 1 Time-lapse of control cells transfected with lifeact-GFP and plated on fibronectin-coated substrates of increasing Young's modulus (2-5-11-14-29 kPa from left to right). Scale bar is 20 μ m.

Supplementary Video 2 Time-lapse of talin 2 shRNA cells transfected with lifeact-GFP and plated on fibronectin-coated substrates of increasing Young's modulus (2-5-11-14-29 kPa from left to right). Scale bar is 20 μ m.

Supplementary note – computational model.

The computational model was developed by adapting a Monte Carlo simulation approach previously described in detail¹. Briefly, the model considers an actin filament being pulled by n_m myosin motors, each of them capable of exerting a force of F_m . In the absence of adhesion to the substrate, this filament moves at a speed v_a , corresponding to the unloaded speed of myosin motors. This filament can use talin-integrin clutches (modeled as springs with spring constant k_c) to bind to a given number of fibronectin molecules n_f . In turn, the fibronectin molecules are all connected in parallel to a spring with spring constant k_{sub} , representing substrate rigidity. At each time step of the simulation, unbound fibronectin molecules are allowed to bind to integrins according to a binding rate $k_{on} = k_{ont} \cdot d_{int}$, where k_{ont} is the true binding rate characterizing the interaction, and d_{int} is the density of integrins on the membrane. Similarly, bound integrins are allowed to unbind according to the unbinding rate k_{off} , which depends on applied force as a catch bond. At the end of each time step the actin filament contracts, dragging the bound clutches and exerting force on each clutch, and on the substrate. Total force on the substrate F is calculated by imposing force balance, and actin speed is recalculated. To recalculate this speed, actin speed is assumed to depend linearly on applied force, ranging from v_a (in the absence of force) to 0 (when the maximum force of $n_m \cdot F_m$ is reached). At this point, the cycle of binding and unbinding starts again. This simulation was run for time steps of 5 ms, until a total of 100 s. After the simulation finished, we converted F and k_{sub} to cell traction stresses and substrate Young's moduli, respectively, by assuming a given adhesion radius r_a as described previously^{1,2}.

In addition to the aspects above, in this work we specifically introduced the modelling of talin unfolding and refolding, and vinculin binding. In each time step, for each bound clutch we calculated the unbinding rate k_{off} , and the unfolding rate k_{unf} for the applied force f . $k_{off}(f)$ was modeled as a catch bond consisting of the sum of two exponentials, one with positive

exponent and the other with negative exponent. The parameters of the two exponentials were obtained after fitting the curve to experimental data from either the fibronectin- $\alpha 5\beta 1$ bond³ or the fibronectin- $\alpha v\beta 3$ bond (Fig. 2a, lifetime data in the figure correspond to the inverse of k_{off}). In both cases, we took experimental data corresponding to the case of maximum activation (with Mn²⁺ ions). Fits shown in figures were obtained by using fibronectin- $\alpha 5\beta 1$ data, but equivalently good fits could be obtained with fibronectin- $\alpha v\beta 3$ data after minor modifications of the parameters. To best fit experimental results, the resulting $k_{off}(f)$ curve was multiplied by a scaling factor of 0.9, possibly reflecting minor differences in experimental conditions between single molecule measurements and integrins within adhered live cells. Additionally, we further increased the unbinding rates of integrin-Fn bonds at very low forces (< 1 pN) with respect to experimental values. Introducing this change only increased the slope at low rigidities, and did not alter any of the other model predictions. The presence of a very high unbinding rate (low affinity) at low forces may reflect a low activation state in integrins not submitted to cyclic mechanical stretch⁴. $k_{unf}(f)$ was modeled as a simple slip bond (one exponential with a positive exponent) by fitting the curve to previously measured data⁵. Because the load on each integrin may be shared between talin and other adaptor molecules, the force used to calculate unfolding was corrected by a factor FR , corresponding to the fraction of integrin-transmitted force experienced by talin. Then, unbinding and unfolding times were determined stochastically according to k_{off} and k_{unf} . If unfolding time was shorter than unbinding time, and fell within the time step window, then talin was allowed to either bind to vinculin (according to a force-independent binding rate k_{vin}) or refold (according to a refolding rate k_{fold}). k_{fold} was also modelled as a simple exponential (with negative exponent) fitted to measured data⁵. If vinculin binding occurred before refolding, adhesion reinforcement was assumed to occur, and integrin density increased by d_{add} integrins/ μm^2 . If integrins unbound before talin unfolding or vinculin binding, integrin density decreased by d_{add} ,

reflecting the fact that adhesions shrink if force application is decreased^{6, 7}. However, integrin density was not allowed to decrease below the basal d_{int} level.

Parameters n_f , k_{ont} , n_m , d_{add} , and FR were adjusted during simulations to fit the different experimental conditions tested. For those parameters, both 95% confidence intervals and sensitivities S were calculated. Confidence intervals were calculated by using the nlparci Matlab function taking as an input the experimental data and the Jacobian matrix of the fitted model function. The sensitivity S was calculated following a previously described approach⁸ according to the following expression:

$$S = \frac{d \log(k_{threshold})}{d \log(p)}$$

Where p are the different parameters, and $k_{threshold}$ is the threshold substrate spring constant (rigidity) that leads to talin unfolding, defined as the point in which integrin density increased by 10% with respect to baseline values. S values can be interpreted as the fold change in $k_{threshold}$ induced by a fold change in parameter value. To calculate S values, $k_{threshold}$ was calculated for p values around the optimal fitted values. Then, $k_{threshold}$ was plotted against p in a log-log scale, and S was taken as the slope of a linear fit to the plot.

References

1. Elosegui-Artola, A. *et al.* Rigidity sensing and adaptation through regulation of integrin types. *Nat. Mater.* **13**, 631-637 (2014).
2. Ghibaudo, M. *et al.* Traction forces and rigidity sensing regulate cell functions. *Soft Matter* **4**, 1836-1843 (2008).
3. Kong, F., Garcia, A.J., Mould, A.P., Humphries, M.J. & Zhu, C. Demonstration of catch bonds between an integrin and its ligand. *J. Cell Biol.* **185**, 1275-1284 (2009).
4. Kong, F. *et al.* Cyclic mechanical reinforcement of integrin-ligand interactions. *Mol. Cell* **49**, 1060-1068 (2013).
5. Yao, M. *et al.* Mechanical activation of vinculin binding to talin locks talin in an unfolded conformation. *Scientific reports* **4**, 4610 (2014).
6. Balaban, N.Q. *et al.* Force and focal adhesion assembly: a close relationship studied using elastic micropatterned substrates. *Nat. Cell Biol.* **3**, 466-472 (2001).
7. Riveline, D. *et al.* Focal contacts as mechanosensors: Externally applied local mechanical force induces growth of focal contacts by an mDia1-dependent and ROCK-independent mechanism. *J. Cell Biol.* **153**, 1175-1185 (2001).

8. Bangasser, B.L., Rosenfeld, S.S. & Odde, D.J. Determinants of maximal force transmission in a motor-clutch model of cell traction in a compliant microenvironment. *Biophys. J.* **105**, 581-592 (2013).